EVALUATION AND DEVELOPMENT OF BETA PARTICLE IMAGERS

by

THOMAS BURWELL BATES

Presented to the Faculty of the Graduate School of

The University of Texas at Arlington in Partial Fulfillment

of the Requirements

for the Degree of

MASTER OF SCIENCE IN PHYSICS

THE UNIVERSITY OF TEXAS AT ARLINGTON

August 2018

Acknowledgements

Thanks to the assistance of Dr. Mingwu Jin for accepting me into his research group. Dr. Jaehoon Yu for allowing me to learn about GEMs and their potential uses, and Kien Nham from University of Texas Southwestern Medical School for providing a work environment and assisting with experimentation.

July 25, 2018

Abstract

EVALUATION AND DEVELOPMENT OF BETA PARTICLE IMAGERS

Thomas Burwell Bates, MS

The University of Texas at Arlington, 2018

Supervising Professor: Mingwu Jin

Compact beta imagers have the great potential for tumor localization for radio-guided treatment interventions thanks, in part, to their natural collimation of beta particles. Their rapid survey capabilities of small areas, on the scale of tens of square centimeters, are important for clinical adoption. In this work we investigate the experimental methods and evaluate the performance of the uniformity, sensitivity, spatial resolution and field of view (FOV) of a hand-held beta camera. Results from this work have demonstrated a high degree of sensitivity and uniformity and a millimeter scale spatial resolution within a FOV close to 1 square centimeter. In addition, we report the progress of the development of a new beta imager using gas electron multiplier (GEM) detectors and discuss the related issues for particle detection.

Table of Contents

List of Illustrations

List of Tables

Chapter 1 Introduction

The complete removal of cancerous tumors has been shown to result in a lower likelihood of reoccurrence of malignant tissues in patients [10]. Therefore, it is preferred to use handheld detectors with a small field of view on the scale of tens of squared millimeters and rapid-scan capability of localized areas in subcutaneous procedures [16] to achieve radiometrically guided surgery or other interventions. The high sensitivity and spatial resolution will lead to identify and extract the malignant cells while avoiding damage to healthy tissue. The concept of using radiation imagers for these procedures has been around since 1942 when Geiger Muller counters were used to localize tumors in breast tissues [16]. Since then, both gamma and beta imagers have been used for both cancer diagnostics and treatment procedures by using water soluble radio-sources which are absorbed more by the tumors than the surrounding normal tissues, creating a distinct contrast to isolate cancerous tumor locations within the body.

Beta Imagers typically preferred over gamma imagers for subdermal operations due to their compact size while attaining a high spatial resolution and sensitivity [1]. The short penetration depth of beta emissions requiring no mechanic collimation leads to a more compact detector size than that could be achieved by gamma imagers. Nowadays, the scintillating cameras are the most prominently used thanks to mature technologies, reliability and low cost. However, the gaseous detectors, such as spatially-resolved gas electron multiplier (GEM) detectors, developed at CERN have shown promise as a possible alternative in this arena [15], in part due to their high gain and capability for single photon or electron detection. Additionally, these detectors have been shown to have a spatial resolutions of 50 microns [4] for individual particle tracking, which can easily be converted into high spatial resolution for medical imaging than that the current scintillating cameras are capable of [7]. In this work we investigate and evaluate a newly

developed beta camera based on a scintillating detector. We also worked toward developing a new handheld medical imager based on GEM currently in use at the Large Hadron Collider.

Chapter 2 Beta Cameras

2.1 Scintillating Beta Camera

Scintillating Beta Camera probes are compact radiation imagers, which are used for radioimmunoguided surgeries and tumor localization [1].

Traditional Beta cameras are composed of a scintillating layer, e.g. thin plastic film, photomultiplier (PM) tube and photo-detector allowing for beta particle imaging while passing through the energetic gamma photons [20]. The recent advance has been the use of solid-state PM (SSPM) and a coincidence trigger system in order to determine the relevant data for image accuracy [7, 14, 13].

The beta camera investigated in this work is made of a scintillating plastic coupled with SSPMs[2]. The dimension of the camera head is shown in Fig. 2-1. It was customized built by IntraMedical Imaging LLC., The specifications of the camera are: field of view (FOV) = 16mmx16mm, image matrix = 32x32 pixels (thereby resulting in a .5mm pixel size), a spatial resolution of 1.5 mm (full-width half-maximum, FWHM), and a sensitivity of ~.0005mCi [2]. The primary goal of this study is to evaluate the camera sensitivity and the spatial resolution and prepare for further pre-clinical imaging studies.

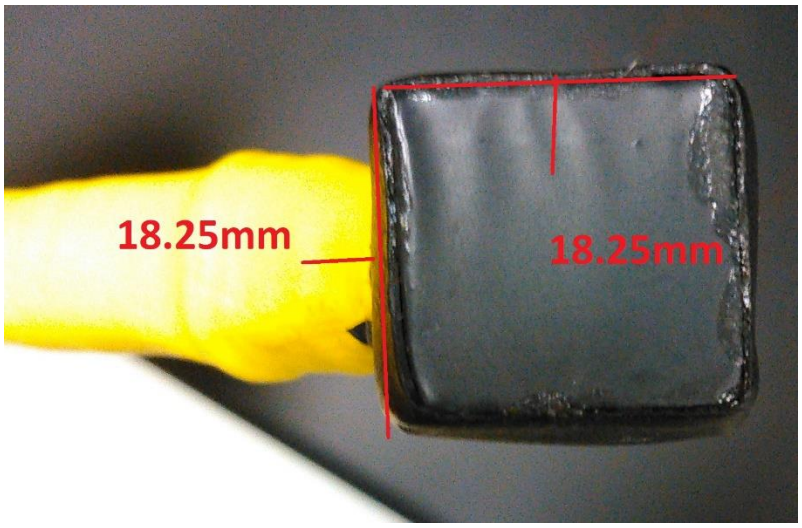

Figure 2-1 Head of the beta camera

2.2 Gaseous Electron Multipliers (GEMs)

Gaseous Electron Multipliers, or GEM's, are fast radiation detection devices created by Fabio Sauli is 1997 for the initial purpose of particle detection in high energy experiments [4]. In the 30 years of since their creation they have demonstrated additional uses in the medical fields of imaging and dosimetry [5, 6, 11].

The detector are composed of a chamber with an ionizable gas, Argon in our case. A Drift plate is placed at the top of the detector with a negative charge applied to it, and placed at various distances are foils, which are comprised of a dielectric medium coated in copper and etched with holed ~50μm in diameter with a pitch of ~50μm, ending in a copper etched readout board at the bottom of the detector [4].

Each side of the foil has a different applied voltage, through the implementation of a voltage dividing circuit. The method by which ionizations are produced and imaged is fairly simple. As the beta particle or x-ray enter the chamber, it passes through the first drift region which then interacts with the atoms of the Argon through MØller Scattering for

electrons, or Klein-Nishina Scattering for photonic interactions, leading to an ionization of the gas. The positive ions are attracted to the negatively charged drift plate at the top of the detector, and the electrons emitted from the ionization are then attracted to a positive voltage drop, created by the aforementioned voltage difference applied to each side of the foils [4]. As the electron nears the top of the foils, this voltage differential combined with the low distance between the copper plating results in a high electric field, on the order of $10^6 \frac{C}{m}$ leading to an avalanche effect of the electrons, effectively multiplying the incident electrons by a scale factor of 100^n where n is the number of foils used. Once the electrons have been ejected through the bottom of the first foil, they then pass through a secondary drift region for additional ionizations. This process is repeated for each foil used in the detector.

After being ejected from the final foil used in the detector, the electrons then approach the final tier of the detector is the layout at the bottom which detects the electrons. This layout board has two possible effective configurations: the first is a layout of strips in the x and y directions by setting a time delay we can observe a refined image of ~50μm [4]. The next possible configuration is an array of pads which creates a 2-D image.

Under the present system there are 124 channels capable of being collecting data for analysis with a 10cmx10cm readout board of a 0.8cm resolution. However, we currently have access to 2cmx2cm foil dimension leading to a, hypothetically, .32mm resolution of the image collected from it. Currently, we need to redesign the readout board and code for image collection in order to retrieve the appropriate images from the detector.

Currently we are using two variants of the GEM detectors, the first configuration of the GEM detector we are using has an active area of 10cmx10cm, with three gem foils with an initial drift region of 5mm, this is roughly 2mm larger than the typical drift region used in most gem labs, the reason for this is the larger the initial drift region the more likely ionizations will occur. Which is shown in Figure 2-2

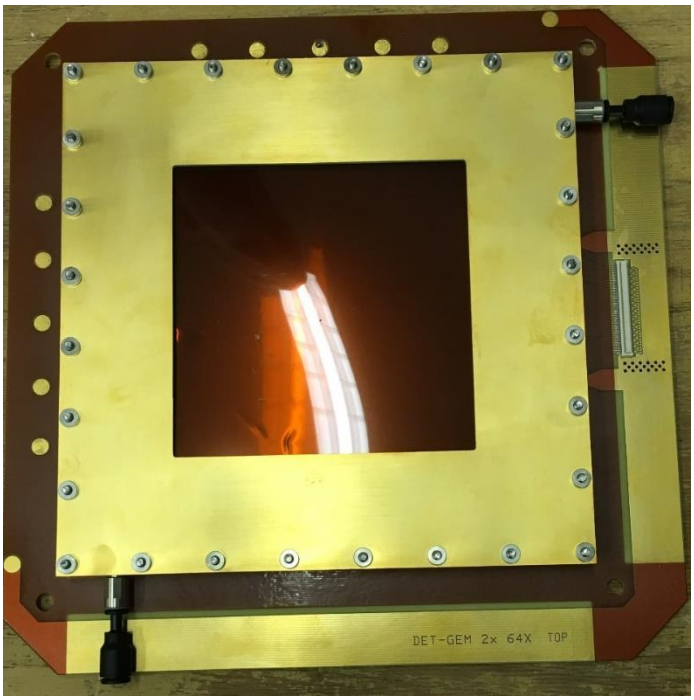

Figure 2-2 Three Layer GEM

The second GEM configuration we have implemented has an active area of 2cmx2cm, this allows us to come closer to our ultimate goal of a handheld GEM detector. To demonstrate this let's look at the image of the detector in Figure 2-3:

Figure 2-3 Two Layer GEM

This GEM detector only has 2 Foils and a single channel copper plate at the bottom, so under the current configuration the most likely use is dosimetry, which has been shown for thick GEM detectors.

2.3 Beta Emitters (Cu64 and Cs137) and Beta Transportation in Matter

For Beta Decay, a radionuclide emits a beta particle (e^+ or e^-) through one of three possible processes. The first is the decay of a neutron, resulting in the emission of an electron, a proton and an anti-neutrino, which can be seen by [18]:

$$\mathrm{n}^0 \rightarrow e^- + p^+ + \bar{\nu}_e$$

Conversely, it is possible for a beta particle to be emitted from a proton converting to a neutron, a positron and a neutrino as well, represented by [18]:

$$p^+ \rightarrow e^+ + n^0 + \nu_e$$

The final type of Beta Decay, is called electron capture, which occurs when an electron is near the nucleus of an atom, a proton in the nucleus then captures the electron and a neutron and an anti-neutrino, presented by [18]:

$$p^+ + e^- \rightarrow n^0 + \bar{\nu}_e$$

Depending on the decay scheme of the radiation source and the intermediary medium, we can calculate a variance penetration depth of each beta particle; for both safety and isolation of relevant data [18].

2.3.1 Calculating stopping distance of the beta particles in matter

In this work, we use beta blocking plates of Aluminum, Al, in each of our experiments, so in order to ensure accuracy, we must look at how beta particles lose energy while traveling through matter. There are two methods by which beta particles lose energy in transport through matter: Coulombic and Radiative losses.

Coulombic losses, also called Linear Energy Transfer (LET), occur from the energy excitations ionizations caused by the Beta particles interacting/colliding with the orbital electrons within the medium. In a sense this is a representation for the damage radiation can cause to biological systems as well [18,19].

Radiative losses occur from the deflection of the Beta particle by the Coulomb field of the nucleus. This causes the Beta particle to emit Bremsstrahlung or Cerenkov radiation thereby causing a decrease in kinetic energy of the particle [18, 19].

These two types of losses by the beta particle are then summed to get the total stopping power of the Beta particle represented by:

$$\frac{dE}{dx} = \left(\frac{dE}{dx}\right)_{col} + \left(\frac{dE}{dx}\right)_{rad}$$

Where:

$\left(\frac{dE}{dx}\right)_{col}$ is the energy loss per unit length for coulomb interactions, and

$\left(\frac{dE}{dx}\right)_{rad}$ is the energy losses by radiative interactions.

Now this is a very general form of the energy lost by a charged particle as it passes through a medium which has a dependence on initial energies, velocities and mass of the beta particle, as well as the density and atomic number of the medium. To determine the LET energy, scattering cross-sections are

L. Katz and A. S. Penfold determined an empirical formula to determine the maximum range of the beta particle regardless of medium which takes the form:

$$R_{MAX} = (.412)\left(E_{\beta}\right)^{1.265-.0954\ln(E_{\beta})}$$

Where, R_{MAX} is the maximum range of the beta particle and E_{β} is the initial energy of the beta particle [3]. Then, the range for a specific medium is the maximum range divided by the density of the medium.

$$R = \frac{R_{MAX}}{\rho}$$

Where R is the Range through the medium and ρ is the density of the medium. Now all that is left is to input the numbers to calculate the maximum values required to block the beta particles, for this we need to look at the decay schemes for both of the sources we used in our experiments, starting with Copper 64, Cu-64, demonstrated in Figure 2-4:

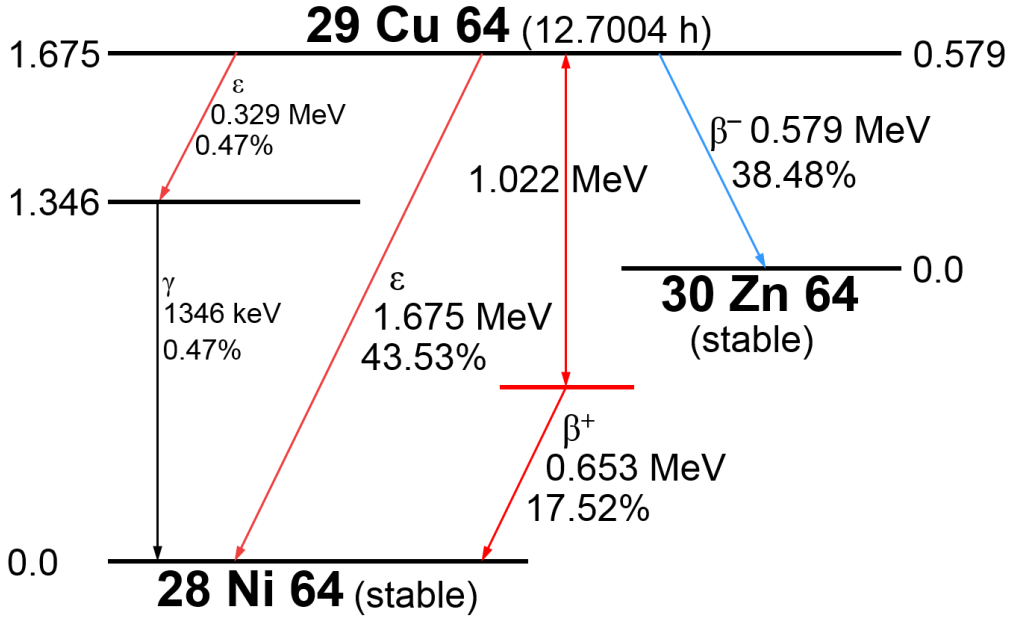

Figure 2-4 Decay Scheme of Cu-64 [18]

So there is a positron, electron and photon decay mode, of which we focus on the positron and electron decay energies. We can now determine the minimum thickness we needed to stop the beta particles from penetrating through the blocker to our camera. This is demonstrated in Table 2-1:

Table 2-1

Medium material	Material density	Energy beta of the decay (MeV)	Maximum range in the material
Aluminum	2.7	.579	0.787826644
Aluminum	2.7	.653	0.913963457

Now that we have isolated the minimum thicknesses required for complete absorption of the beta emissions. But we now need to look at the decay scheme for the

Cesium 137, Cs-137, source we use for later experiments, especially since the energy emissions have a magnitude that is higher than the maximum energy of the beta particle emitted from our Cu-64 source. So, let's look at the Cs-137 decay scheme represented by Figure 2-5:

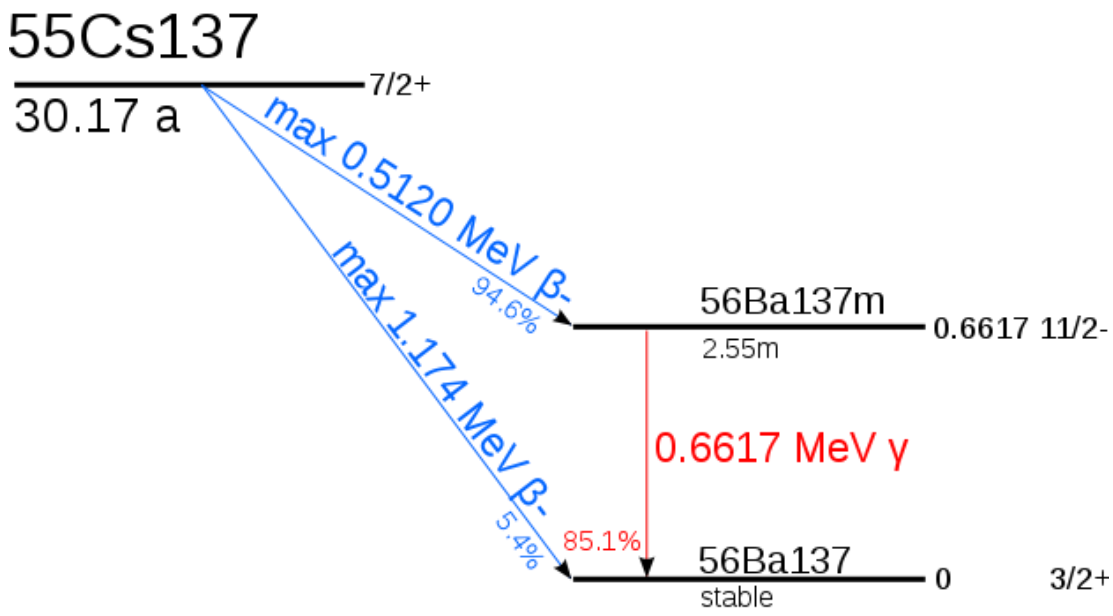

Figure 2-5 Cs-137 Decay Scheme [18]

As we can see from Figure 2-5 the maximum value of the energies of the beta emission is almost 3 times the value of the maximum emitted energy of Cu-64. Now in a similar fashion to the Cu-64 source we can determine the maximum range of the beta particles incident on the blocker.

Table 2-2

Medium	Density (g/cm^3)	Energy (Mev)	Range in medium (mm)
Aluminum	2.7	.5120	0.676021648
Aluminum	2.7	1.17	1.835949772

Now that we have the maximum range through an Aluminum medium calculated, we now know the minimum thickness we require for our blockers.

Chapter 3 Experiments for the scintillating beta camera evaluation

In order to test the capabilities of the Beta camera, we preformed three types of experiments: to evaluate uniformity sensitivity, a 2-dimensional (2D) spatial resolution test, and a field of view (FOV) test.

3.1 Uniformity/Sensitivity Test

The first order of business to test is the total counts and uniformity of the beta camera in order to isolate problematic pixels in the detector. Should there be a significant deviation from the expected uniformity result compared to, similar experiments [9], the outlying pixel count should be identified, extracted and discarded in all future experimentation. Additionally, the manufacturer should be informed, as to avoid similar future issues.

To determine the uniformity and sensitivity of the Beta Camera, we set up an optical rail system with a maximum length of 50cm, with the camera stationed at one end of the rail. Then, we positioned a point source which can be seen in Figure 3-2, in direct contact with the camera, demonstrated in Figure 3-3, and collected 30 total images at a rate of 2.5 images/s (i.e. 400ms per image).

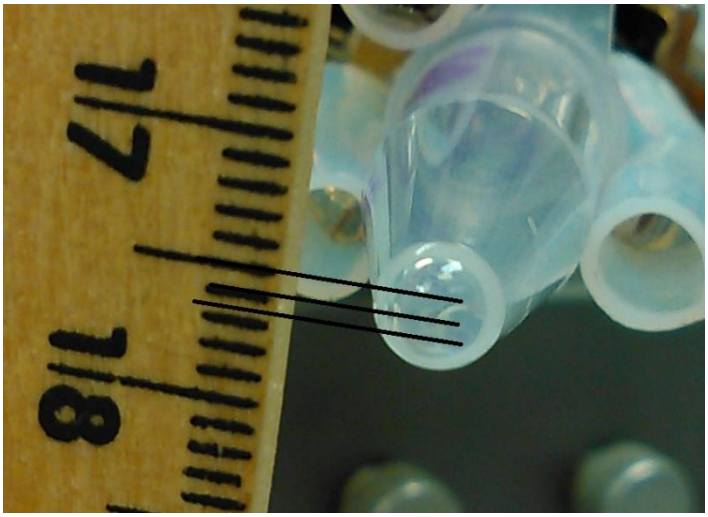

Figure 3-1 The point source of Cu-64, whose diameter is ~1.5mm

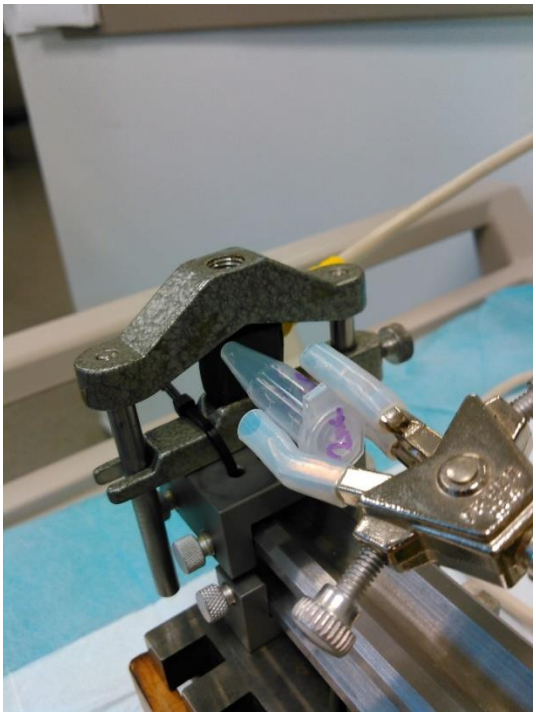

Figure 3-2 Initial data collection configuration for the source in contact with the camera

Then, we shifted the source away from the camera by ~5cm and collected 30 images again (see Figure 2-3), this process was repeated until reaching a maximum distance between the camera and the source of ~45cm.

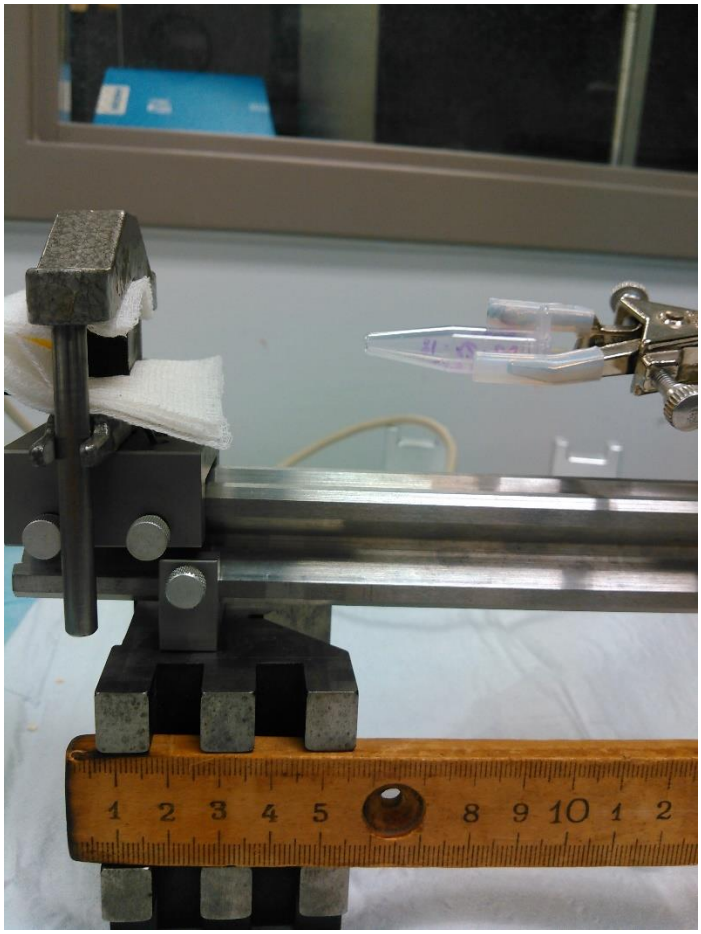

Figure 3-3 The data collection configuration for the source at 5 cm distance from the camera

The general principle for this test comes from the radial nature of radioactive emissions. As the distance between the source and the camera increases two things will occur: First the total counts of all pixels in the image from detector will go down due to the decreased geometric efficiency. Second the difference between the counts of each pixel

should decrease leading to a higher uniformity since the emitted beam from the source approaches the parallel direction similar to a uniform flood source.

We then preformed a secondary experiment to look at the edge spread function of the image which requires part of the camera being blocked allowing for imaging of a sharp edge.

We preformed this experiment with blockers made with three different materials: aluminum, wood, and plastic. The source was placed at ~5cm from the camera and the images were collected from each blocker.

3.2 2-D Spatial Resolution experiments

To verify the camera spatial resolution provided by the manufacturer, we used a Cu-64 flood source with an initial activity of .17mCi, with a source container shown in Figure 2-4. The top lid of the source container is 0.6mm to ensure the sufficient beta particles to pass through.

Figure 3-4 Source Container

We used a series of 2.4mm thick aluminum plates with arrays of holes with varying hole diameters and spacing which can be seen in Figure 3-4. These plates were then placed on top of the source box in Figure 3-4, with the camera is fixed directly above the plate.

Since, the field of view for the camera is 16mmx16mm according to the manufacturer and the largest size of the array of holes in each plate is ~21.25mmx~21.25mm, the camera should be able to produce noticeable intensity spikes at regular intervals which should correspond to at least 58% of the array area. Where the imaging dimensions are calculated by:

$$\frac{16 * 16}{21.25 * 21.25} * 100\% = \sim 58\%$$

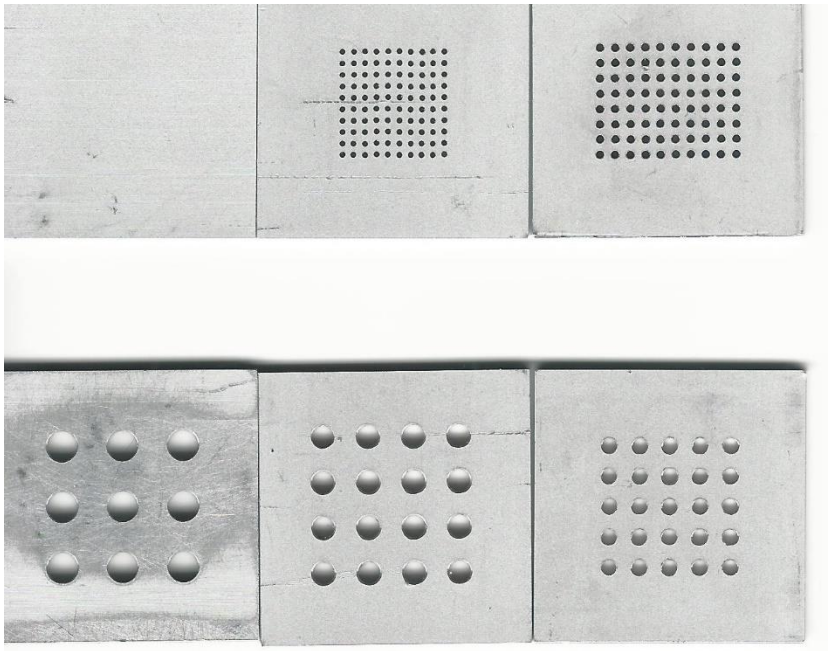

Figure 3-5 Plates used for 2-D Spatial test, from top right to Bottom Left we have Full Blocker, .75mm holes, 1mm holes 4mm holes, 3mm holes, and 2mm holes

30 images were collected for each plate at a rate of 2.5 images/second. The images were then averaged to provide a less noisy image.

We also preformed an additional experiment to measure the edge spread function of the image to derive the modular transfer function (MTF), which requires part of the camera being blocked. The MTF will be used to determine the spatial resolution of the camera. Both horizontal and vertical resolution will be investigated [12].

3.3 Field of View Test

While we were performing the spatial resolution experiments, images collected appear to have a smaller FOV than the specification provided by the manufacturer. One example is shown in Figure 3.6. As can be seen, in both the x and y direction we can only identify three intensity peaks at most, which correspond to the holes in the plate. It implicates that the camera's field of view is not as large as the manufacturer specification (1.6 mm x 1.6 mm). Other examples for 2mm-hole and 4 mm-hold plates are shown in

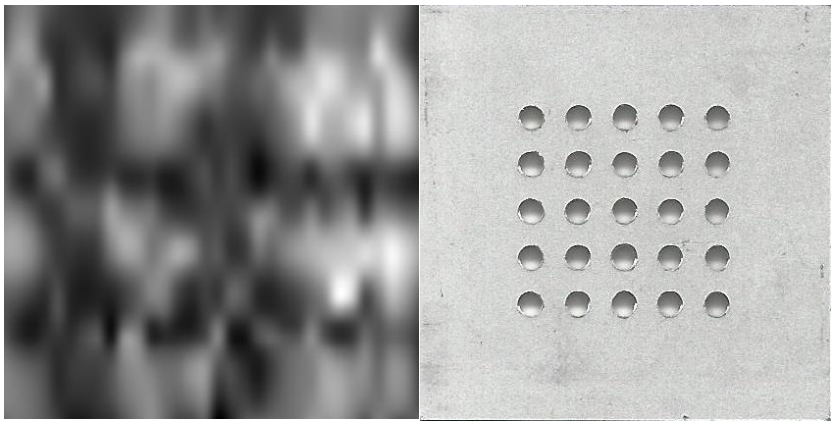

Figure 3-6 Left Image collected from the Camera, Right the 2mm hole plate used

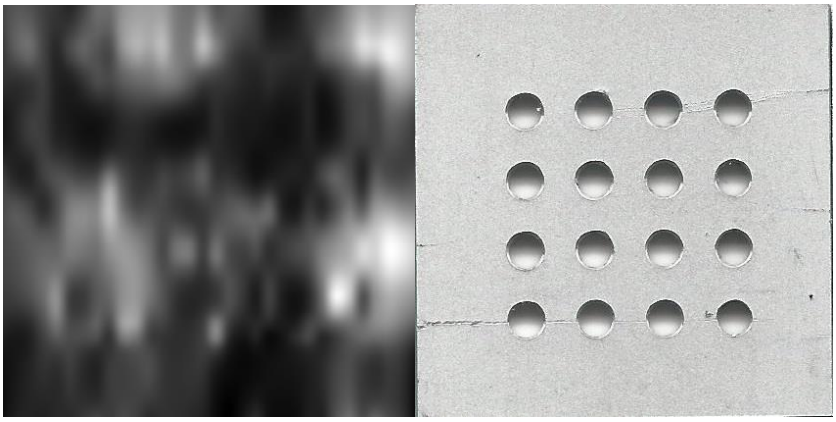

Figure 3-7 Left Image collected from the Camera, Right the 3mm hole plate used

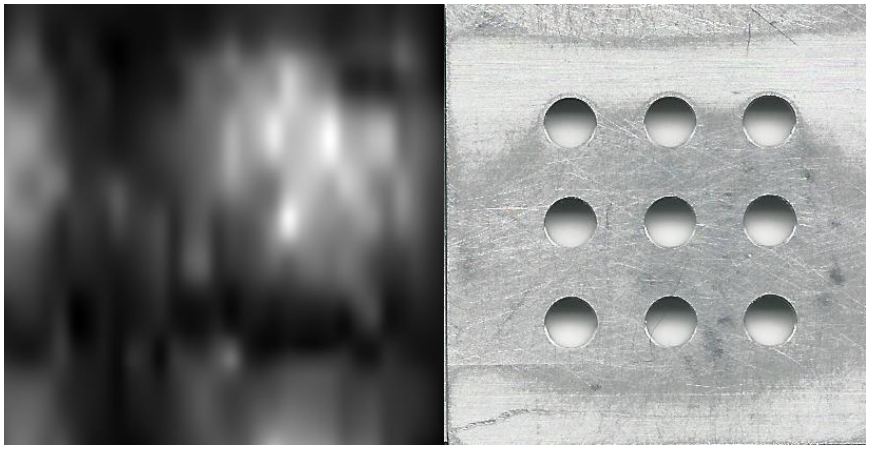

Figure 3-8 Left Image collected from the Camera, Right the 4mm hole plate used

From Figures 3-6 through 3-8, the FOV is roughly a quarter of what we would expect by assuming a 16mmx16mm field of view. As such, it became necessary to determine the actual camera field of view, the results of this experiment tie into the spatial resolution test as well since we need a proper conversion factor between the detector pixel dimensions and the image dimensions to find the spatial accuracy.

To perform the FOV test, we suspended the beta camera above a sealed Cs-137 source and collected 30 images for the normalization (Figure 2-13 left). Then we placed an aluminum plate over the source and as close to the camera as possible, so that the source is totally blocked for another 30-image acquisition. Next, we shifted the blocked at increments of 1mm from one end to the other in order to find where the active area of the camera.

The initial set-up of the distance measurement sets the ruler to 51 at the edge of the collimator and the outside edge of the plate to 58.2cm as a zero axis, i.e. where the source is completely unblocked, ~5mm from the position of the camera head. Which is presented in Figure 3-9:

Figure 3-9 Left: initial image collected for the unblocked source in the x-direction; Right: Initial image collected for the unblocked source in the y- direction

With the left image representing image collection along the x-axis, and the right image representing the image collection along the y-axis. The blocker is then shifted by

5mm inward to block part of the camera head and images are then collected again. This process is then repeated until the blocker has been removed to the other side of the camera. For a total of 13 data points.

Chapter 4 Analysis of Experimental Data

There are a few preliminary processes to be implemented to prepare for data analysis. The first step is to collect images for the camera without a source present to preform a dark light calibration of the camera. However, when we ran the collection software for this case no images were collected regardless of the setting of the camera. It seemed that there was some mechanism implemented in the camera to set the dark light images less than a certain threshold to be zero.

Next, we did average over the thirty images for the following analysis, unless otherwise stated, although the analysis of each individual image can be applied likewise. The raw data from the camera for a flood source is shown in Figure 4-1 as an example. As can be seen, there are some non-effective areas and possibly scaling factors in x and y directions. Thus, it is necessary to crop and interpolated the initial image in order to reflect the real active area (FOV) and dimension of the camera. Additionally, the image is not uniform with hotspots which appear to be the locations of the siPMs. Indeed, the flood source image shall serve as a normalization map for images acquired by the camera to maintain the uniformity. The cropping, interpolation, and normalization of Figure 4-1 is shown in Figure 4-2.

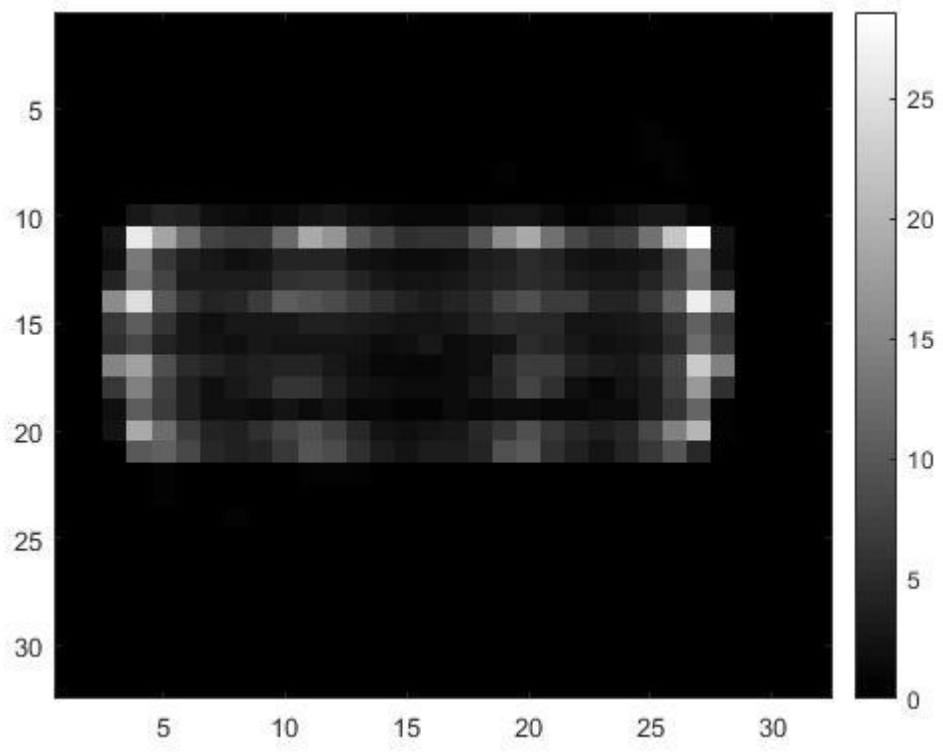

Figure 4-1 Raw averaged image collected from the camera

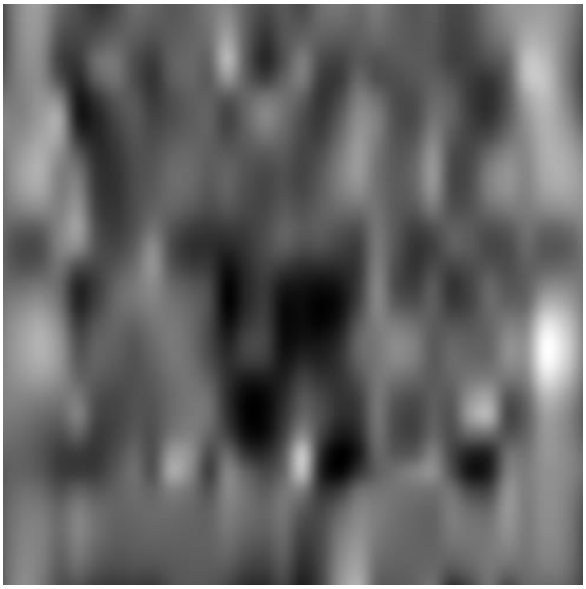

Figure 4-2 Cropped image from the source shown in Figure 4-1

After these pre-processing steps, we can move on to the analysis methods for evaluation of different metrics.

4.1 Uniformity/Sensitivity

The uniformity of each image from a flood source is defined as:

$$U = \frac{\Sigma\left|\mathrm{f} - \bar{f}\right|}{\Sigma f} * 100\%$$

where $f(i)$ and $\bar{f}$ represent the count value at ith pixel and the averaged image values over the whole image under observation [9].

For the sensitivity analysis, each pixel was summed to provide the total event count the camera recorded for each measurement taken:

$$TC = \sum_{i=1}^{n} f(i)$$

Where, f(i) is the count at the current pixel, and n is the total number of pixels in the image.

Then, to determine the spatial resolution, a line is taken perpendicular to the edge identified in the image, which is then plotted in a 1-D intensity plot creating the, edge spread function (ESF). A derivative is then taken of the ESF to calculate the line spread function, LSF, of the image [8, 12]:

$$\frac{dI}{dx}(ESF) = LSF$$

Where I is the intensity of the plot at each point. Then a fast Fourier transform is applied to the LSF to determine the modular transfer function (MTF) [8, 12].

4.2 2-D Resolution

Data using the hole patterns

As shown in the last chapter, the spatial resolution data collected should provide images with clearly distinguishable holes, whose 2-D intensity distribution can be model as a Gaussian function. First, the images collected for the plates with different hole sizes are examined to see whether some hole patterns could be distinguished from the background. In Figure 4-3, the beta image of the aluminum blocker plate (without holes) is shown along with the picture of the plate. As expected there are no clear intensity spikes for this image, however we are still getting some counts, which contradicts results from the fact that beta particles should be totally blocked. It suggests that the camera may have picked up some gamma photons to form the image. Beta images with different hole sizes (0.75 mm, 1 mm, 2 mm, 3 mm, and 4 mm) are shown in Figure 4-4 to 4-8. As we can see from these images, Figures 4-3 through 4-6 have hole sizes which are too small to create the clearly defined peaks we would expect so we will confine our analysis to Figures 4-6 to 4-8.

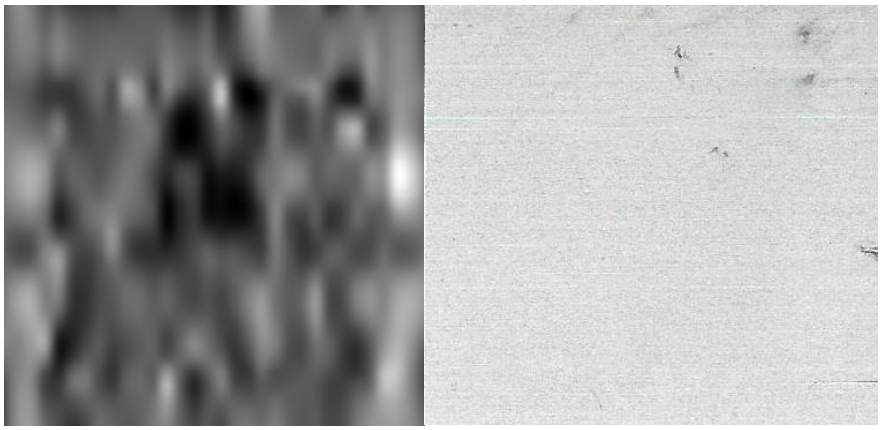

Figure 4-3 Beta image (left) of the full blocker plate (right)

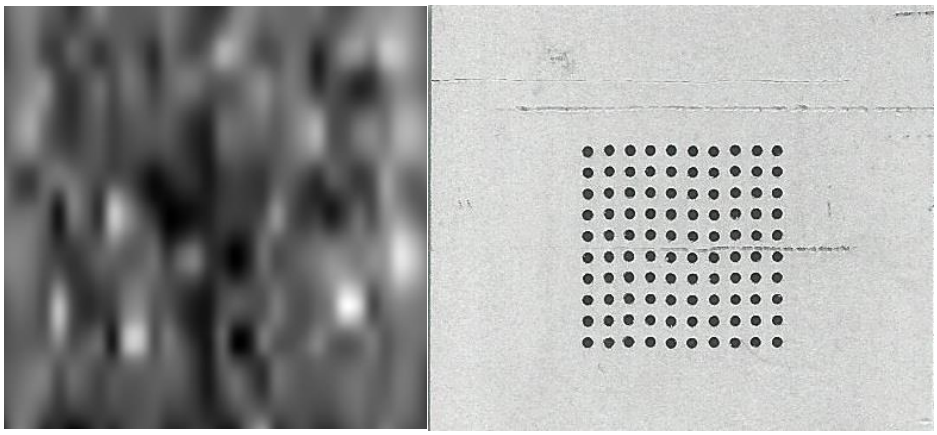

Figure 4-4 Beta image (left) of the .75mm plate (right)

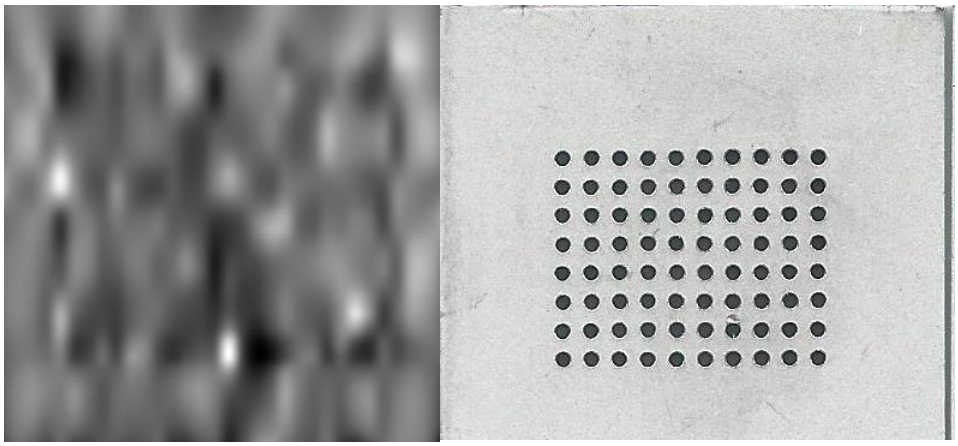

Figure 4-5 Beta image (left) of the 1mm plate (right)

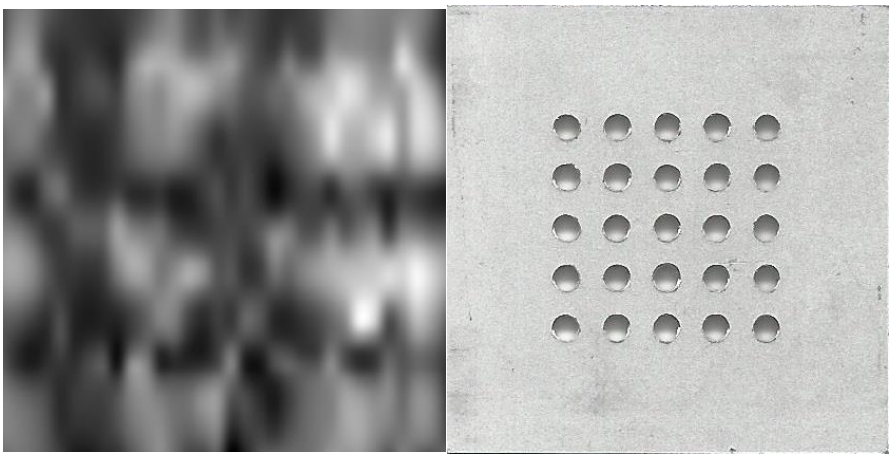

Figure 4-6 Beta image (left) of the 2mm plate (right)

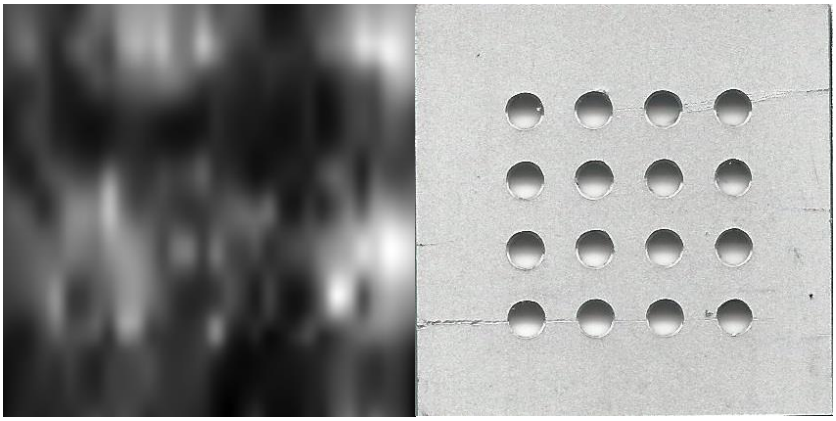

Figure 4-7 Beta image (left) of the 3mm plate (right)

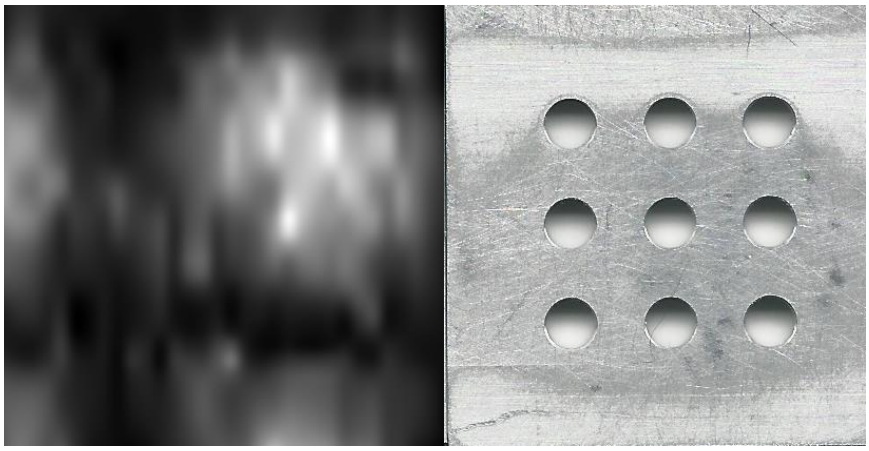

Figure 4-8 Beta image (left) of the 4mm plate (right)

The next step is to isolate the indices of the column and row that represents the center of the hold. Initially, we thought the best way to carry this out is to get the indices of the highest intensity value automatically, thereby isolating a region of interest. However, the signal had a tendency to be noisy and the highest intensity value did not necessarily occur at the centers of the holes. So, we further visually examined the images to identify the hold centers. The resulting hole centers are shown as the crosshairs in Figures 4-9 through 4-11.

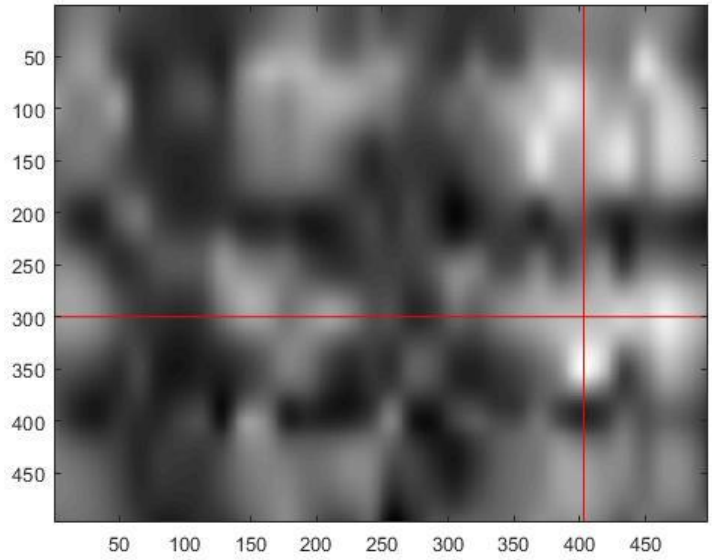

Figure 4-9 The location of the hold center for the 2mm hole plate

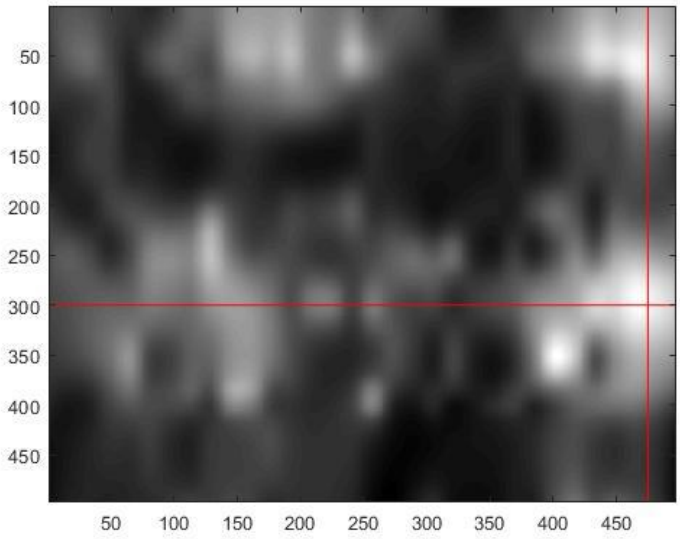

Figure 4-10 The location of the hold center for the 3mm hole plate

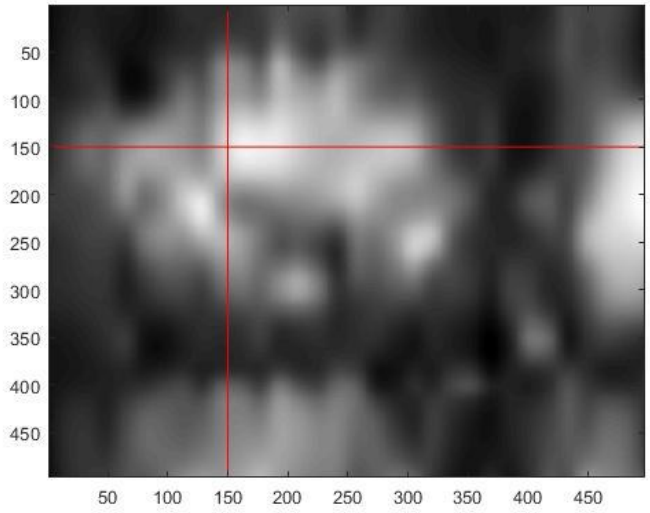

Figure 4-11 The location of the hold center for the 4mm hole plate

With the location of the hole centers, presumably the peak of the Gaussian distribution, the Full-Width Half-Maximum (FWHM) values can be calculated to represent the spatial blurring effect of the camera, i.e. the indictor of the spatial resolution. The method used to calculate the FWHM will be to fit the 1D hole profile to a Gaussian function and calculate FWHM using the estimated standard deviation σ following FWHM = 2.335 σ.

Data using the sharp edge

Finally, we have the Edge Spread Function (ESF) [8,12] determination using sharp-edge images in order to get the Modular Transfer Function (MTF) for the spatial resolution. First, the images of a sharp edge of the blocker are taken by the beta camera. The 1D intensity profiles perpendicular to the edge are average to get the ESFs. The derivative of the ESF is then taken to produce the Line Spread Function (LSF). Finally, a Fourier Transform is then applied to the LSF to get the MTF.

4.3 FOV

For the Field of View test we initially preformed a qualitative study of the holes identified from the spatial resolution test working under the assumption that the spatial resolution was accurate for all plates with distinguishable holes. What we then did is to count the number of holes identified in the image and compared to the length of that number of holes on the raw plate in order to provide an approximation of the Field of view in each direction. This was done with plates with distinguishable hole patterns.

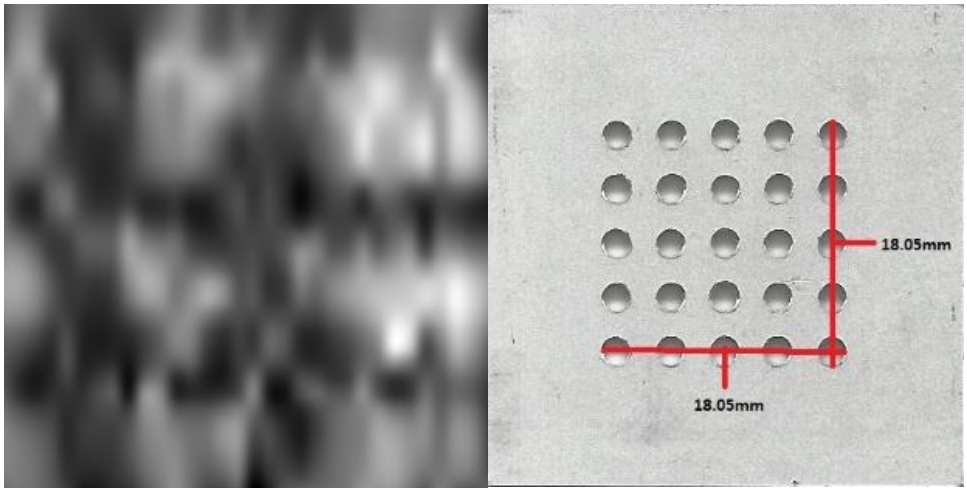

Figure 4-12 Beta image (left) of the 2mm plate (right)

Now we can see from Figure 4-12 that the highest number of hotspots, i.e. holes, we can see is ~2.5 in both the horizontal and vertical direction. This implies the FOV of the camera in each direction is ~ 9 mm x 9mm (half of 18.05 mm). This implicates the camera has an active area about ~50% of the camera head. We also confirmed this finding by examining 3-mm and 4-mm holes as shown in Figure 4-13 and 4-14. Both of them confirm the previous finding of 2-mm holes for a camera FOV about 9 mm x 9 mm.

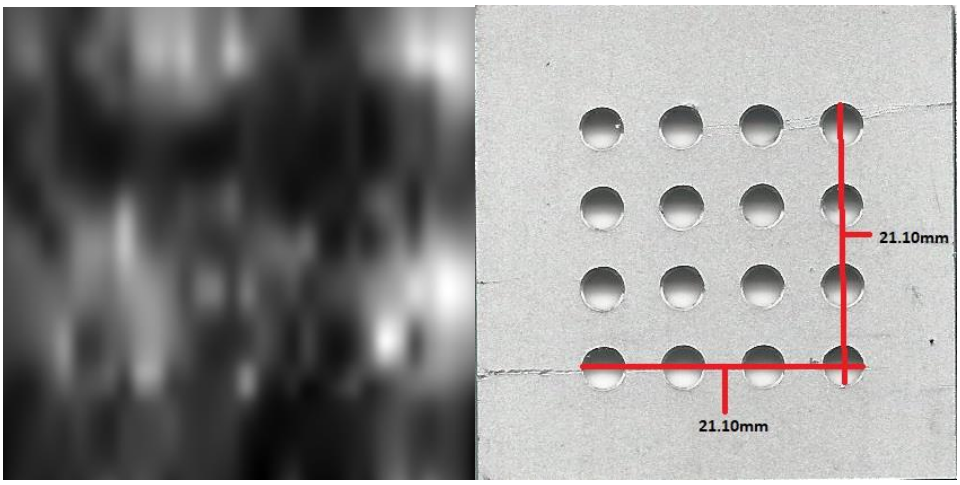

Figure 4-13 Beta image (left) of the 3mm plate (right)

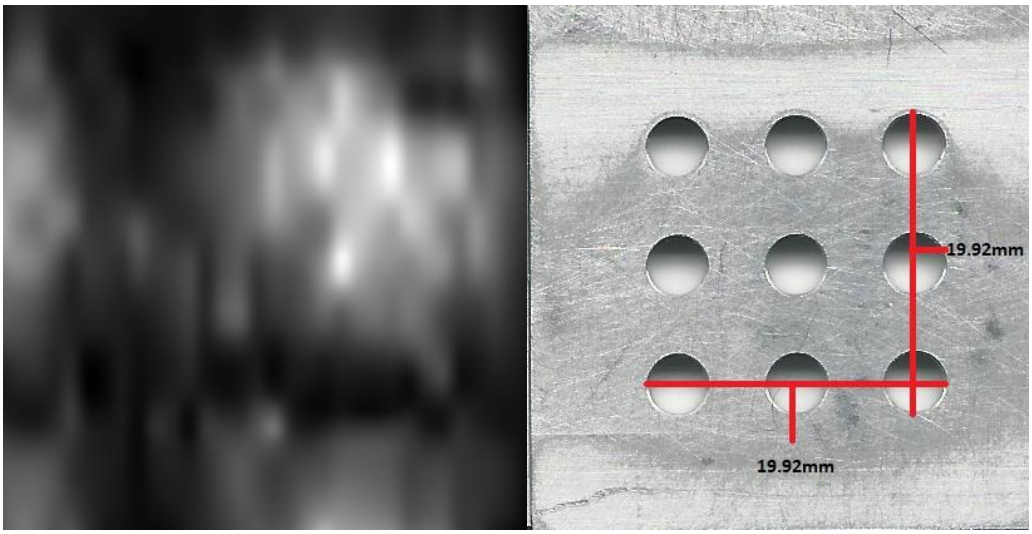

Figure 4-14 Beta image (left) of the 4mm plate (right)

The qualitative study provides a rough approximation of the FOV. A more quantitative study is conducted by shifting the blocker in mm. For this we focused on retrieving the total averaged counts from the images collected at each point of the blockers movement. The idea is as the blocker begins to block the active area of the detector, there would be a significant drop

in the total counts received. The total counts versus the distance shifted will form a 1D box shaped profile. From this profile, the active area (FOV) of the camera can be obtained.

Chapter 5 Results

5.1 Uniformity/Sensitivity

The sensitivity and the uniformity at different distances of the beta camera are shown in Figure 5-1.

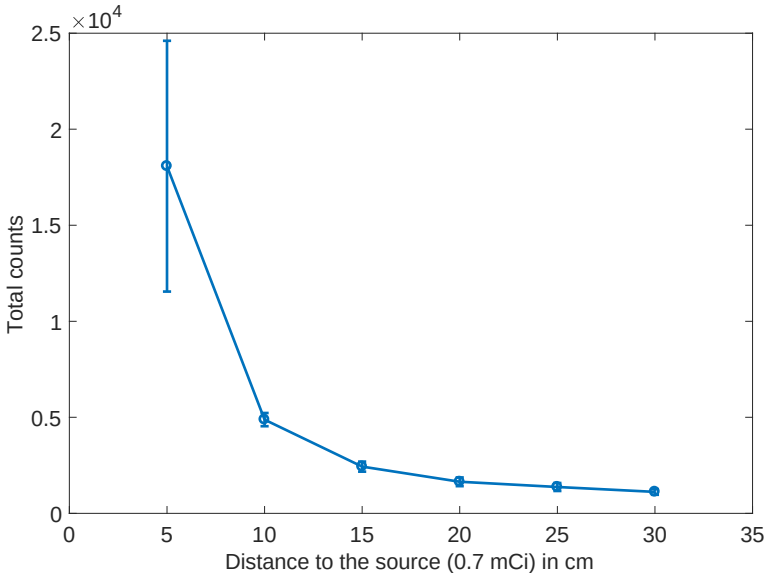

Figure 5-1 Sensitivity of the camera at different distances from the source.

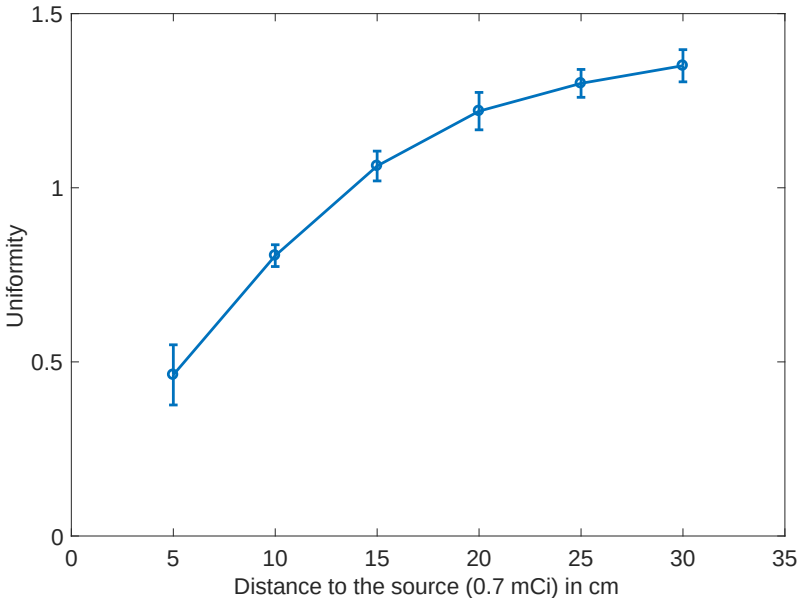

Figure 5-2 Uniformity of the camera at different distances from the source.

As we can see from Figures 5-1 the sensitivity appears to be decaying quickly, as the geometrical efficiency shall follow the inverse square law of the distance and the beta particles exponentially attenuated by the medium. While Figure 5-2 appears to be acting as a logarithmic growth function i.e. the differences between the pixels and the average values of each pixel are decreasing thereby becoming more uniform. There is one aspect we noticed during the experiment which we have not covered here. As the distance between the source and the camera increases, the time required to take the thirty images appears to increase despite the setting for the trigger was set to follow the internal clock of the computer, i.e. 1 picture every 400 ms. Thus, there seems a minimum count number that dictates the image acquisition. This issue can be only resolved with the help from the manufacturer.

5.2 Spatial resolution

Modular Transfer Function

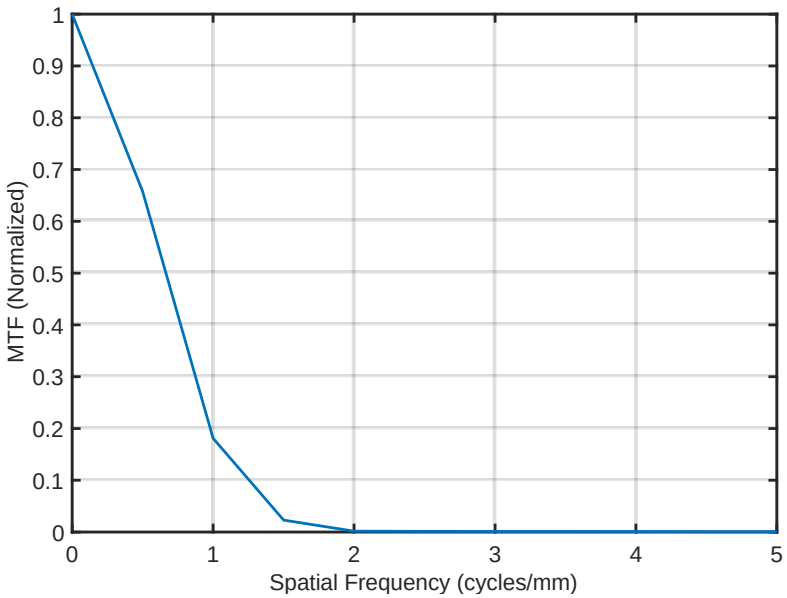

Figure 5-3 modular transfer function of all three blockers

Here we have the results for the Modular Transfer of all three Blockers the overall shapes of each one are so close together that we are unable to distinguish them from each other. Plus, the characteristic curve we are seeing fits with the expected shape of the MTF.

Hole patterns

All images are interpolated to 500 x 500 to avoid undersampling. The line profiles of 2-mm holes (whose locations are in Figure 5-4) are shown in Figure 5-4. The red triangles denote the peak locations and the blue squares the trough location. These points were used to isolate the individual hole image for the calculation of FWHM. The similar plots for 3-mm and 4-mm holes can be found in Figure 5-5 to 5-6.

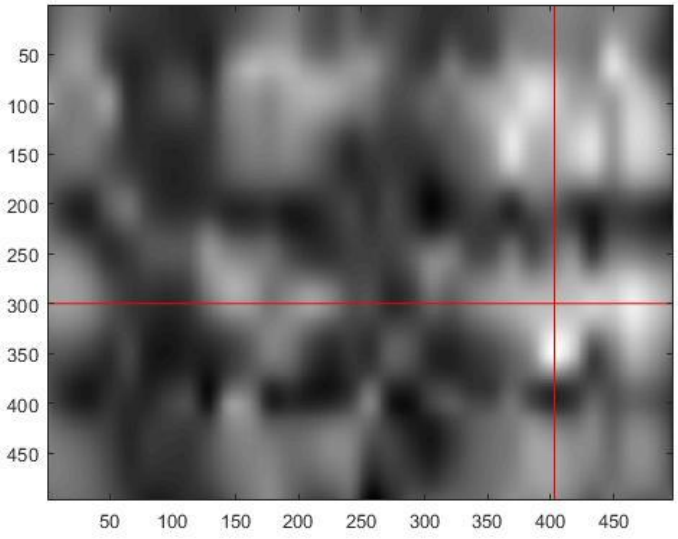

Figure 5-4 The location of the hole center for the 2mm plate

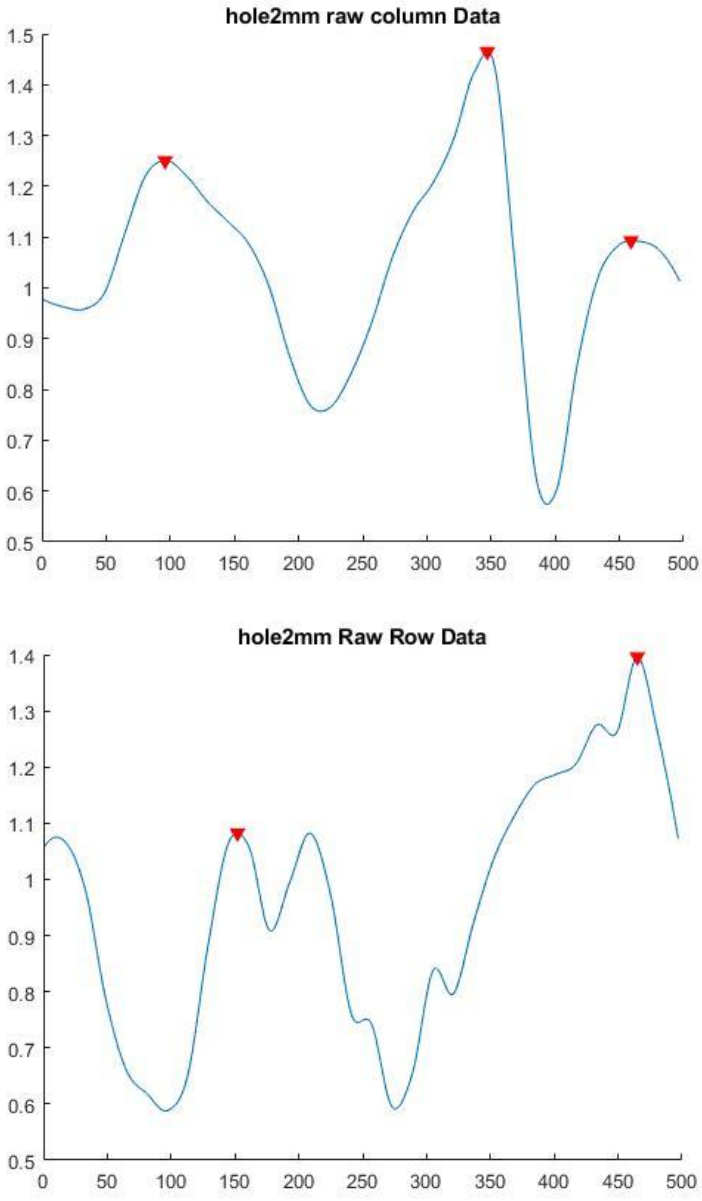

Figure 5-5 The horizontal intensity profile (top) and the vertical profile (bottom)

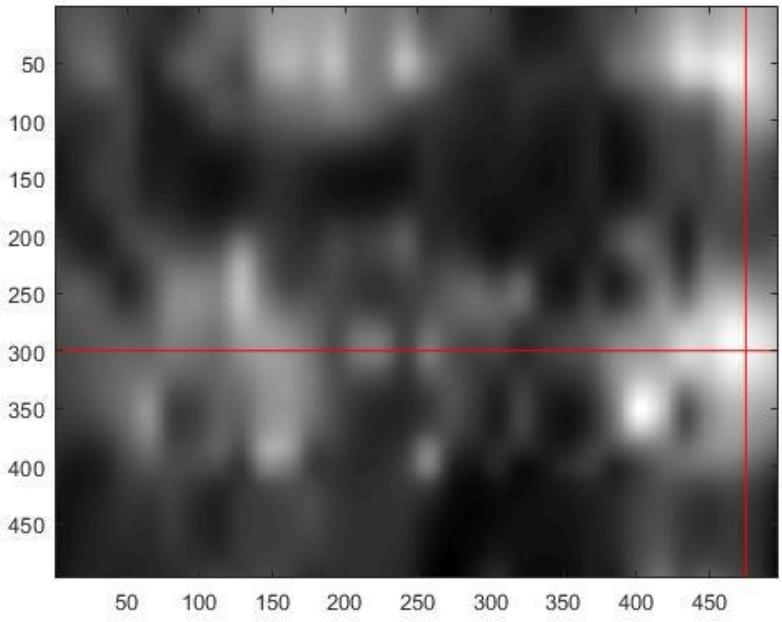

Figure 5-6 column isolation of the 3mm column and row

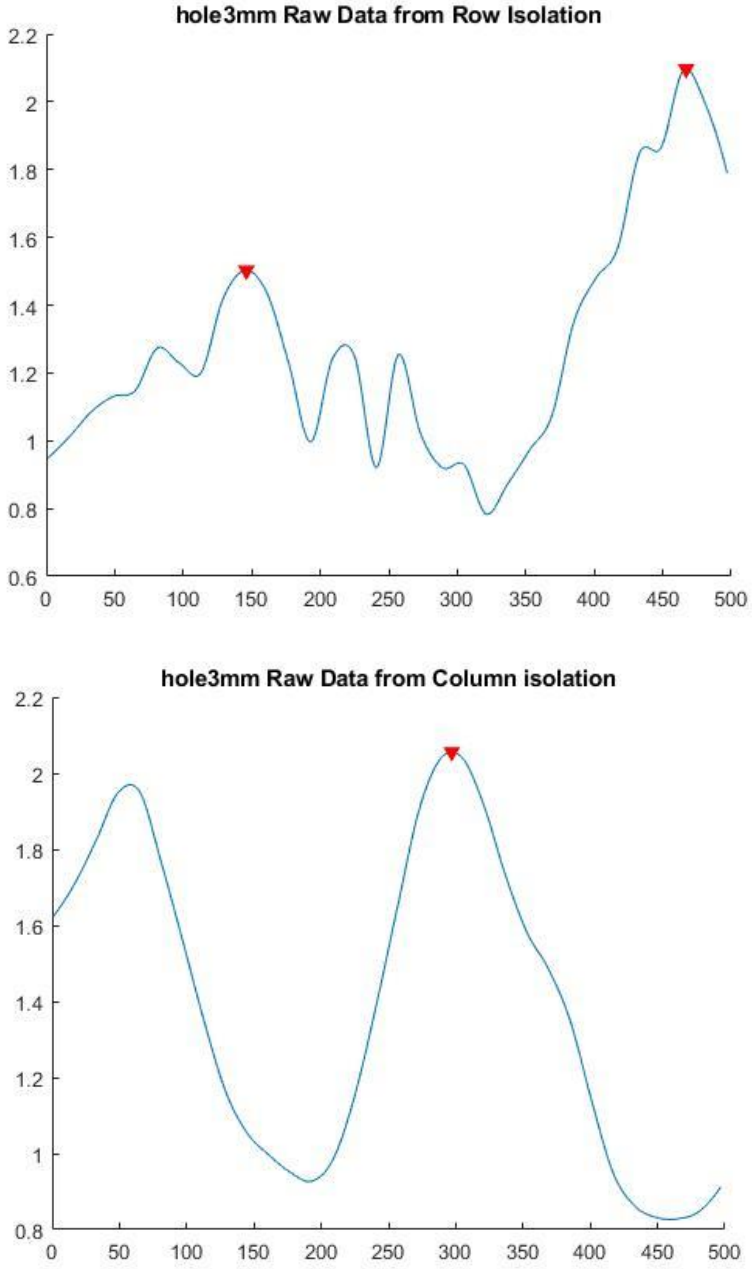

Figure 5-7 The horizontal intensity profile (top) and the vertical profile (bottom)

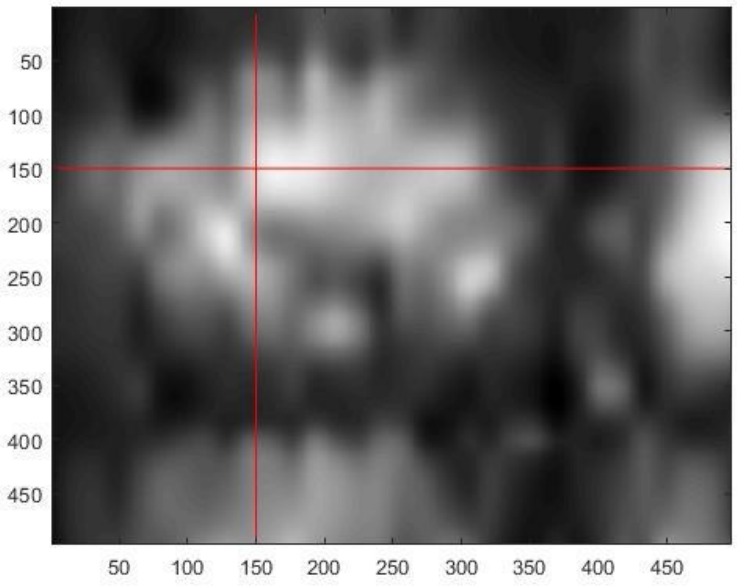

Figure 5-8 column isolation of the 3mm column and row

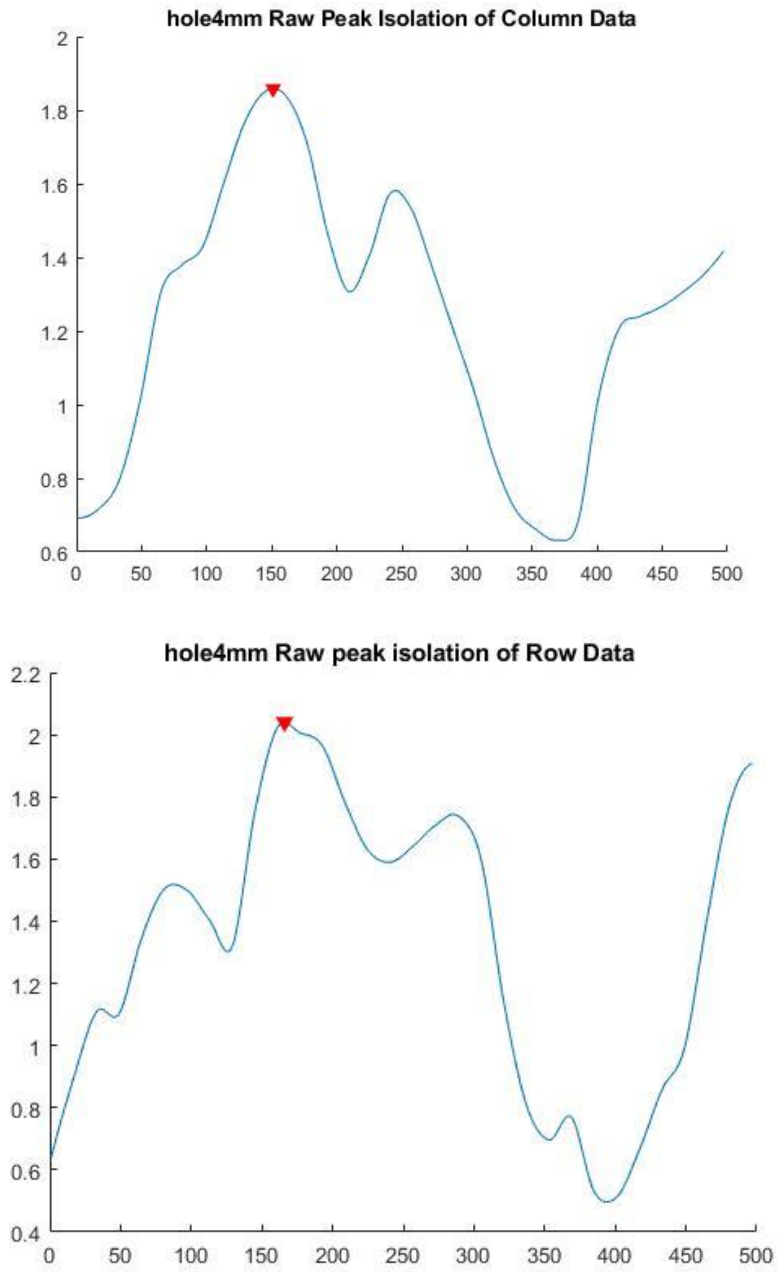

Figure 5-9 The horizontal intensity profile (top) and the vertical profile (bottom)

As can be seen, the line profiles are negatively impacted by noise. Thus, the Gaussian smoothing is applied to mitigate the influence of noise. Afterward a single hole profile (with the

most pronounced peak) is isolated using the peak and trough locations as shown in Figure 5-10, 5-12, and 5-14. Finally a gaussian fitting (Figure 5-11, 5-13 and 5-15) is applied to determine the corresponding FWHM value presented at the top of these plots (labeled as FWHMX). There are about 6% difference for the 2-mm hole, 0 different for the 3-mm hole and 1% difference for the 4-mm hole, between the horizontal and vertical FWHM values. Percent differences between interpolated pixel are calculated by the following equation:

$$\%\, difference = \frac{n(i) - \bar{n}}{\bar{n}} * 100$$

Where, $n(i)$ and $\bar{n}$ are the number of pixels at the ith instance, and the average number of pixels counted for each plate.

These results imply there is a similar image resolution along these two orthogonal directions. The further rotational symmetric of the camera can be assumed.

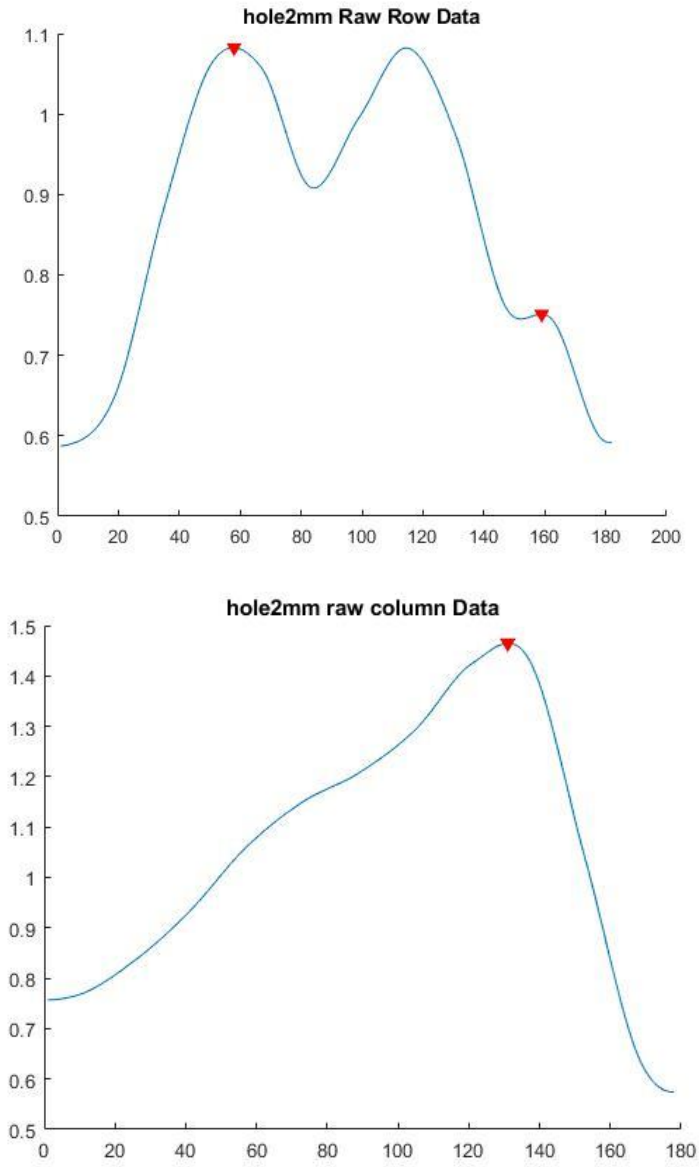

Figure 5-10 The isolated horizontal line profile (top) and vertical profile for a single hole for the 2mm plate

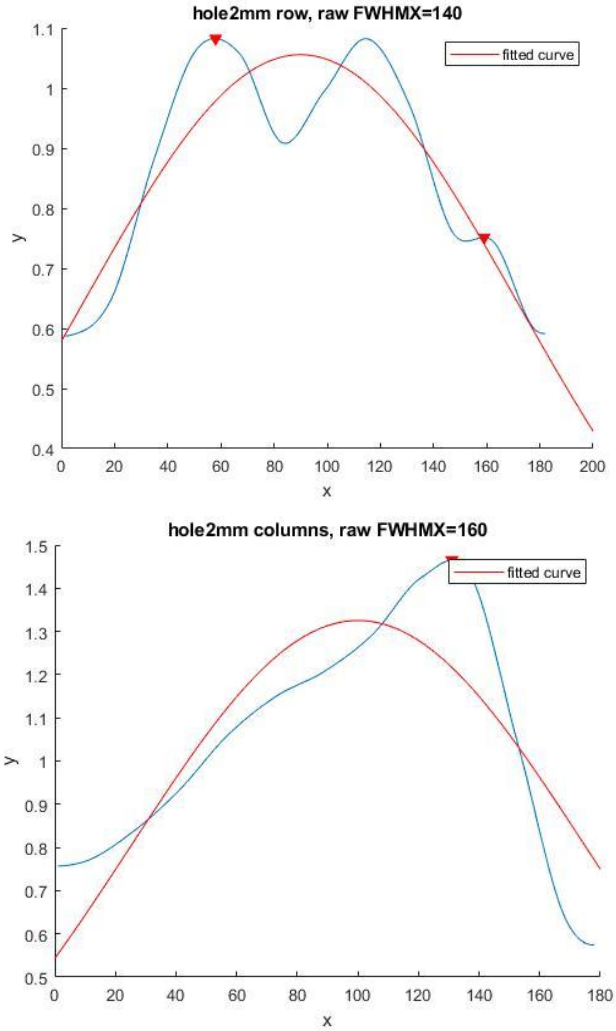

Figure 5-11 The Gaussian fitting of the line profiles of the 2mm plate

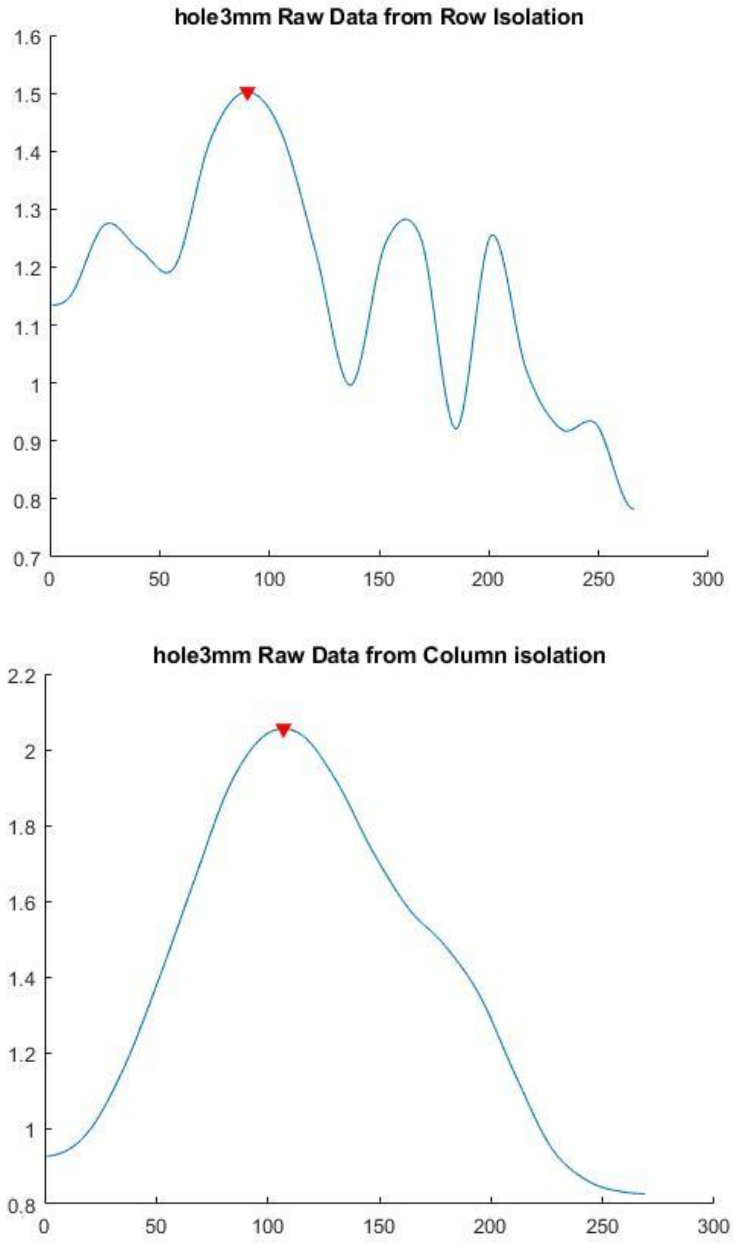

Figure 5-12 The isolated horizontal line profile (top) and vertical profile for a single hole for the 3mm plate

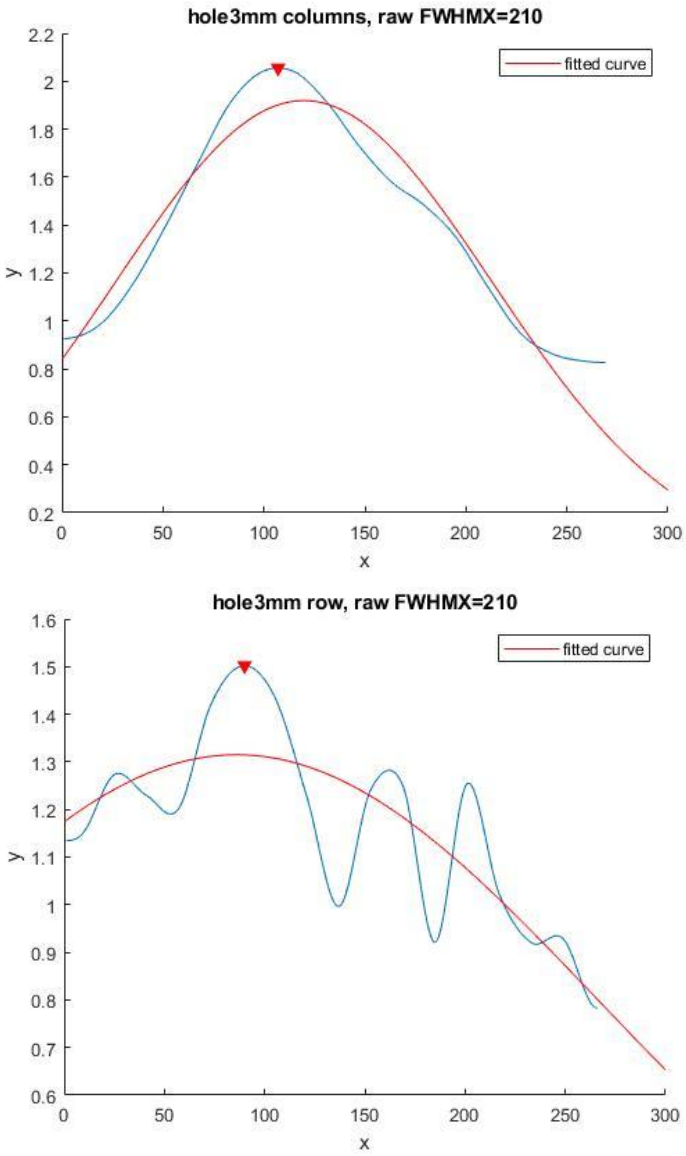

Figure 5-13 The Gaussian fitting of the line profiles of the 3mm plate

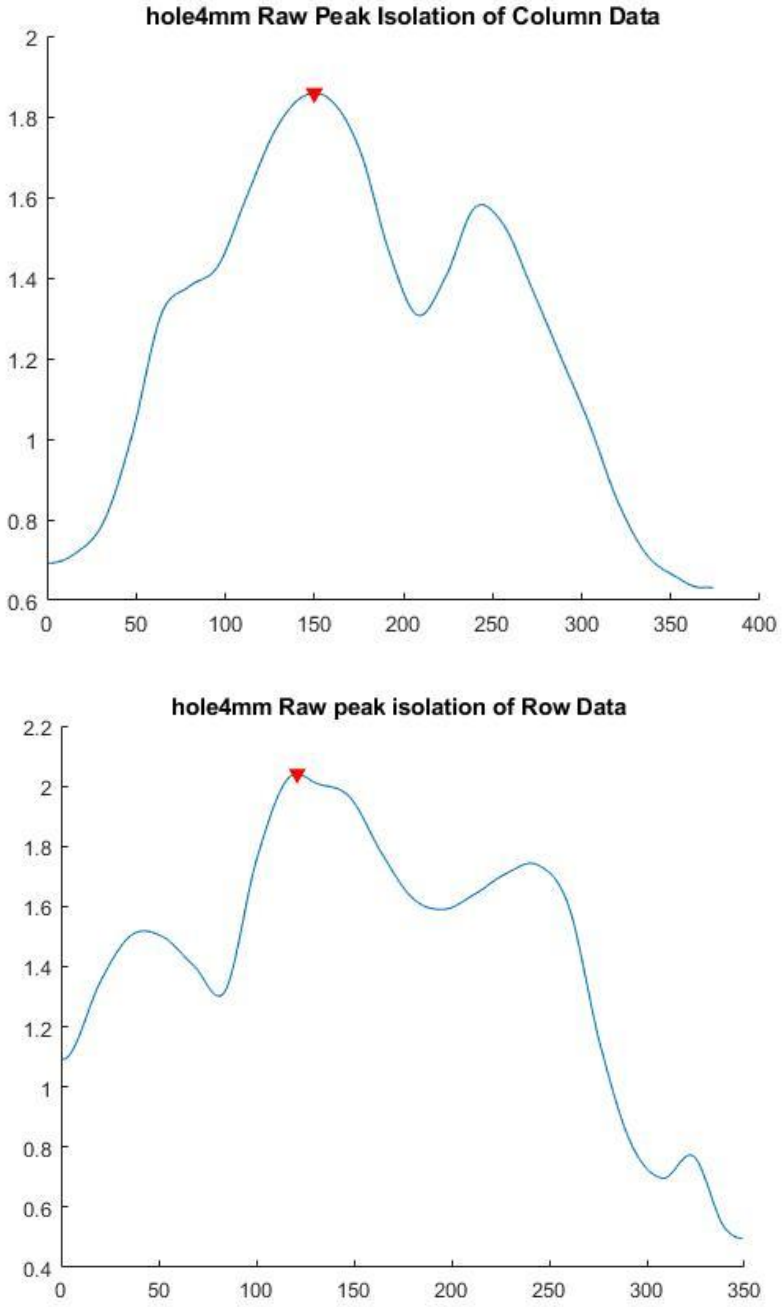

Figure 5-14 The isolated horizontal line profile (top) and vertical profile for a single hole for the 4mm plate (bottom)

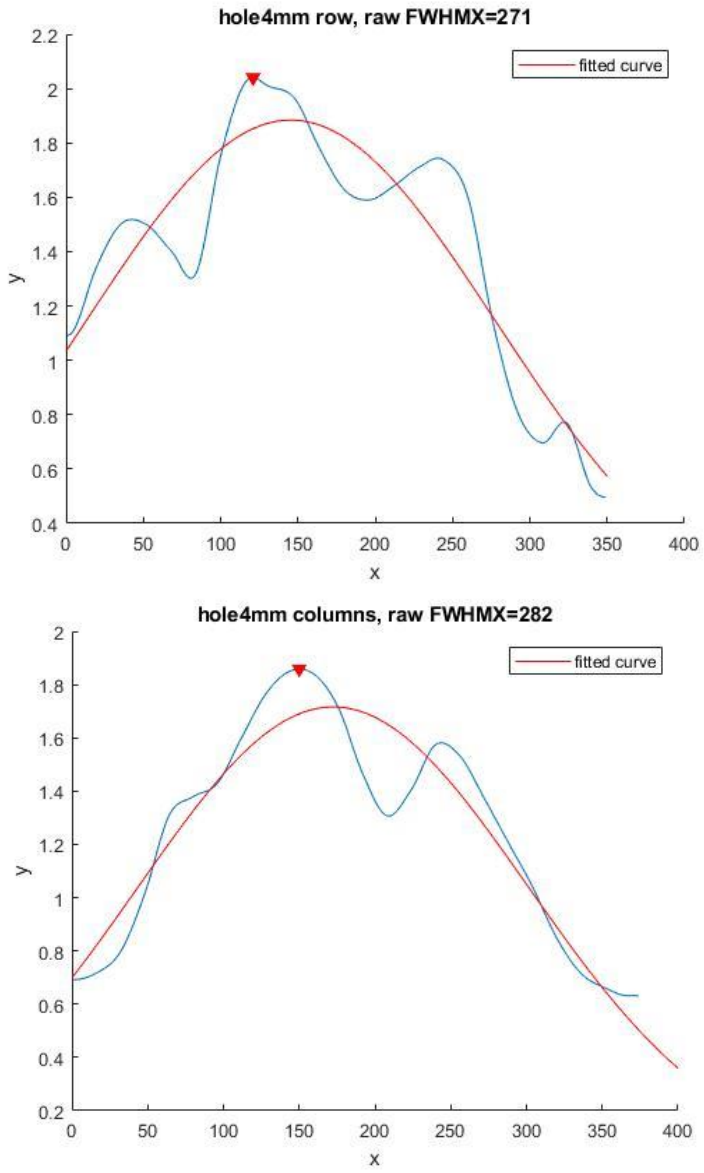

Figure 5-15 The Gaussian fitting of the line profiles of the 4mm plate

Next, we convert the number of pixels of FWHM to mm. Since the image matrix is interpolated into 500 x 500 for a FOV of 8 mm x 8 mm, the size of each pixel can be calculated as

$$pixel\ size = \frac{8\ mm}{500\ pixels} = .018 mm/pixel$$

The corresponding FWHM values are listed in Table 5-1. It seems that the camera has a 25% spread of the actual sizes of imaging objects (except for 44% of the horizontal FWHM of 2-mm hole).

Table 5-1

Diameter of Holes (mm)	Horizontal		Vertical	
	Number of points in plot	Value after conversion(mm)	Number of points in plot	Value after conversion(mm)
2	160	2.56	140	2.24
3	210	3.36	210	3.36
4	271	4.336	282	4.512

ESF method

One example of the sharp-edge images is shown in Figure 5-16. The edge of the blocker can be clearly seen with minor noise on the blocked side, which could be attributed to gamma radiation penetrating through the blocker.

Figure 5-16 The beta image of the vertical edge (for estimation of the horizontal resolution)

The edge spread function (ESF) is shown in Figure 5-17, which demonstrates a graduate intensity transition from the blocked region to the unblocked region. This is the consequence of the step function (of the sharp edge) blurred by the camera response function. By taking the derivative of ESF [8, 12], the line spread function (LSF) is obtained as shown in Figure 5-18. The line with blue circles is the derivative of the raw data and the solid read line is a Gaussian fit of the raw derivative in order to alleviate the noise influence. The modulus of the Fourier transform of LSF leads to the Modular Transfer Function (MTF) [8,12] as shown in Figure 5-19, where the 10% MTF resolution is about 1.8 cycles/mm. The results for the vertical ESF, LSF, and MTF are shown in Figure 5-17 to 5-23. The 10% MTF resolution is about 2.2

cycles/mm. These results seem to be consistent with 2-mm hole FWHM results (Table 5-1), i.e. the vertical resolution is better than the horizontal one.

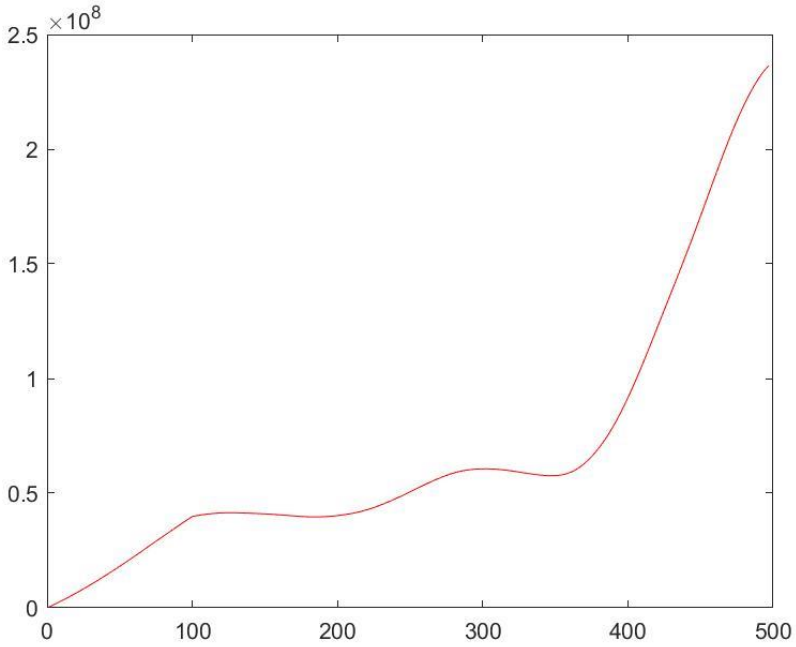

Figure 5-17 The horizontal edge-spread function (ESF)

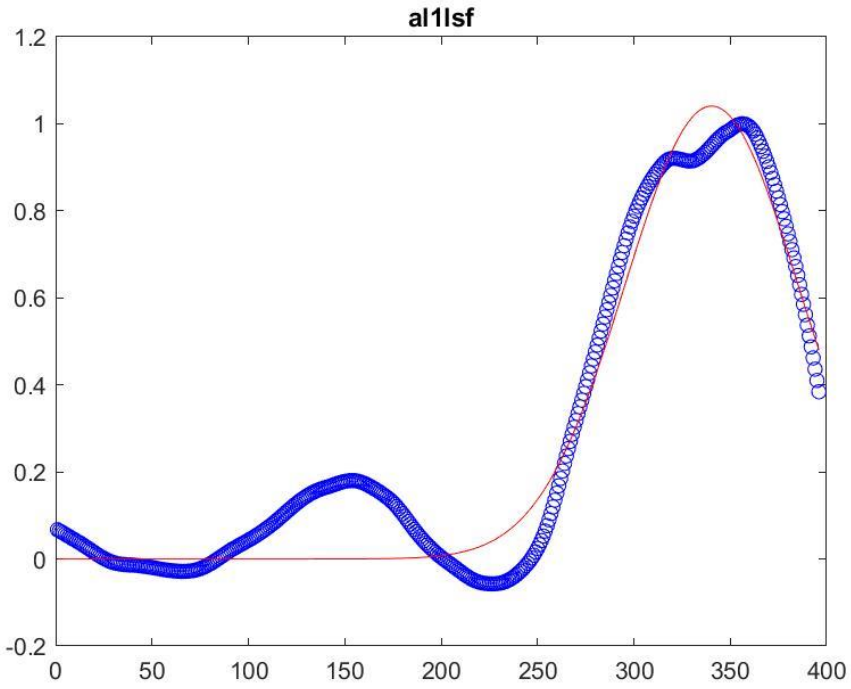

Figure 5-18 The horizontal raw (blue) and fitted (red) line spread functions (LSFs)

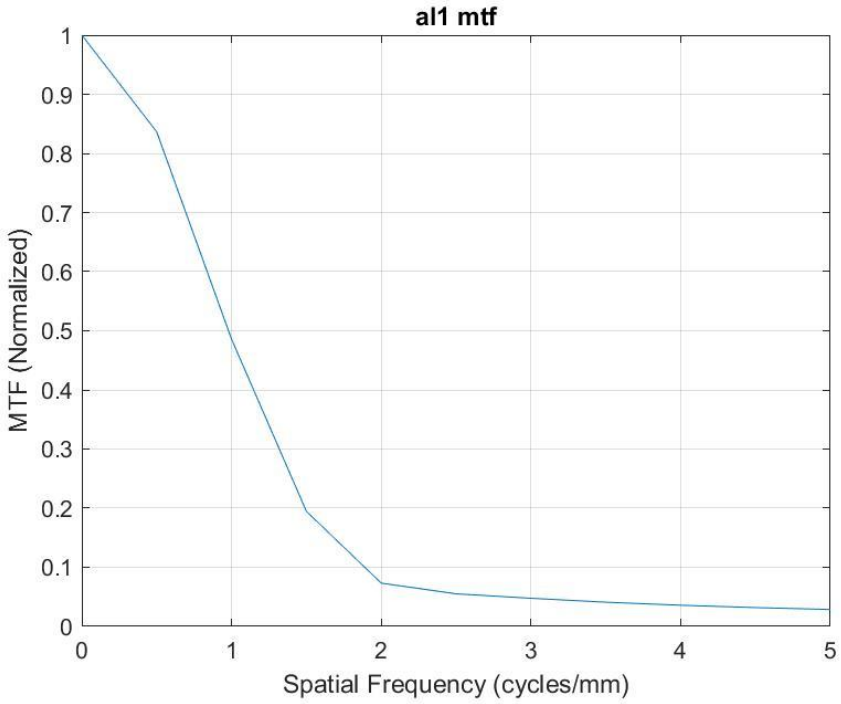

Figure 5-19 The horizontal modulate transfer function (MTF)

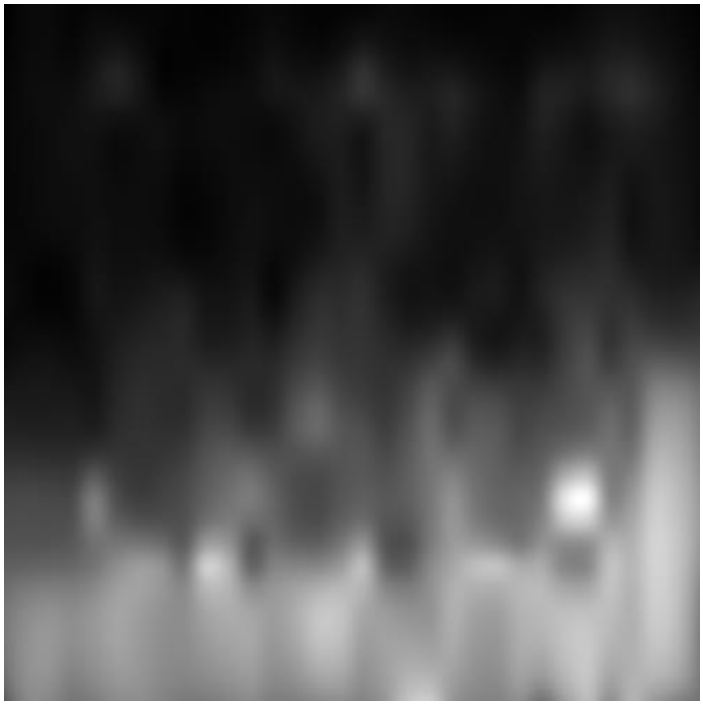

Figure 5-20 Vertical edge image

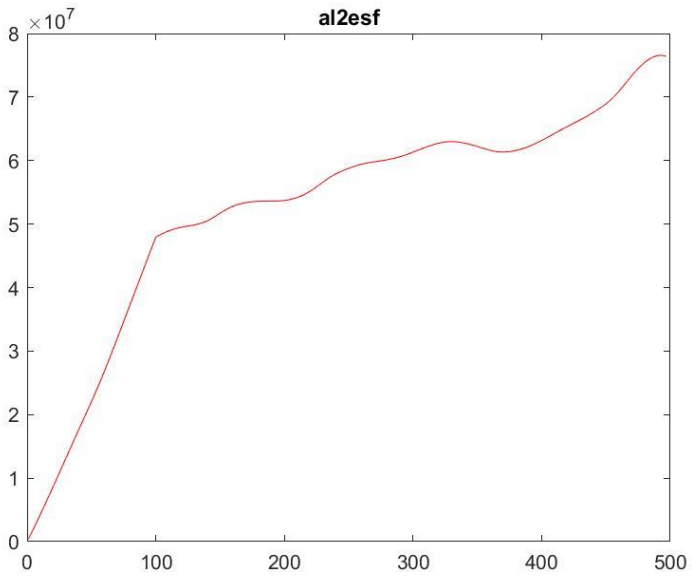

Figure 5-21 Vertical Edge Spread Function

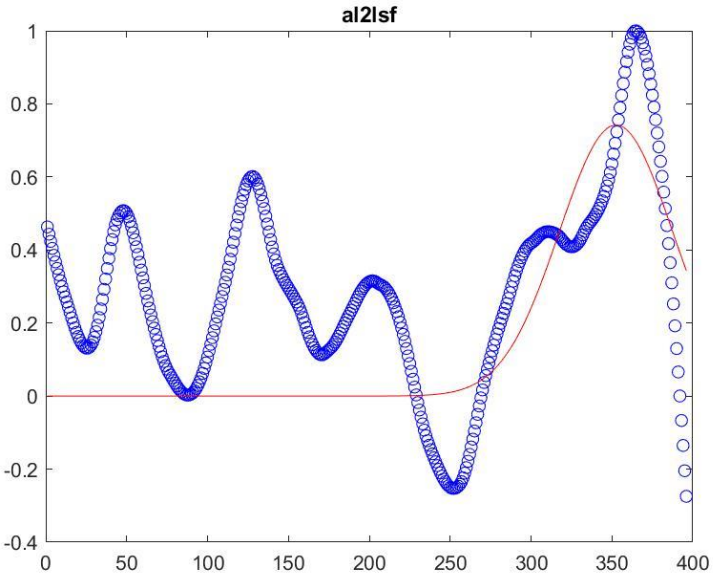

Figure 5-22 Vertical raw (blue) and fitted (red) line spread functions (LSFs)

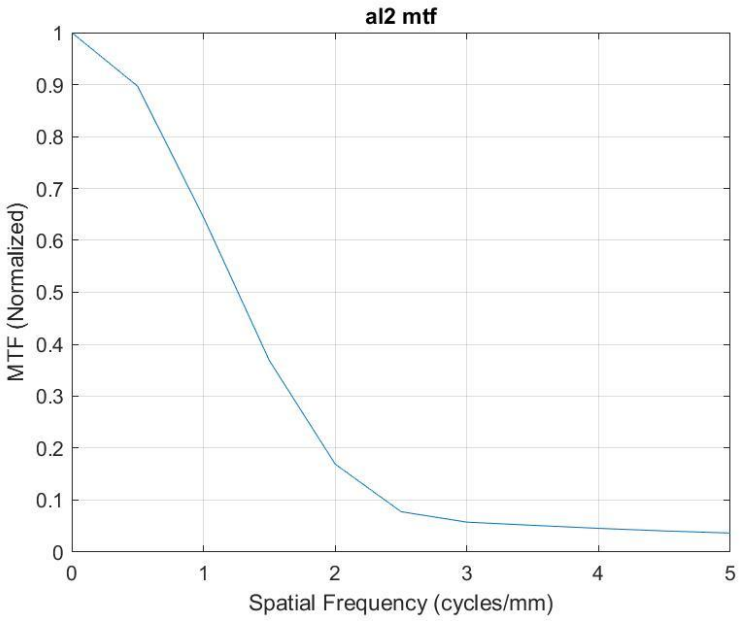

Figure 5-23 Vertical modulate transfer function (MTF)

5.3 FOV Results

The total counts received by the camera as the blocker moving from one end to the other are shown in Figure 5-24. Instead of a valley box, a peak box profile is observed. This is the inverse of what we expected. One possible explanation is that the beta camera was set to collect images at a rate of 2.5 images/s. However, we noticed a ~300% discrepancy between the times required to collect the images with and without the blocker. When the source is completely unblocked, the images are collected every once every 400ms while the blocker is in place the images are collected every ~1.5 seconds. This appears to confirm the issue in the code for the data collection software identified in the uniformity experiments. Nevertheless, the plateau of the plot in Figure 5-24 indicate an inactive area about 3 points into the edge of the camera, equivalent to 5 mm (Figure 5-25). These results suggest that the FOV of the camera is 8mm x 8mm, which is consistent with the number deduced from the hole patterns in Chapter 4 (9 mm x 9mm).

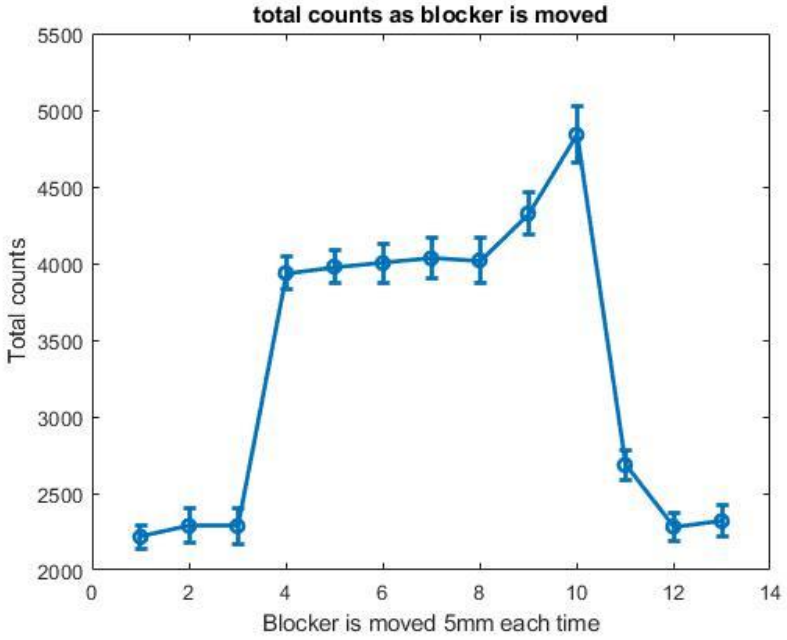

Figure 5-24 The total counts received as the blocker shifted from one end of the camera to the other (each point corresponds to 5 mm shift)

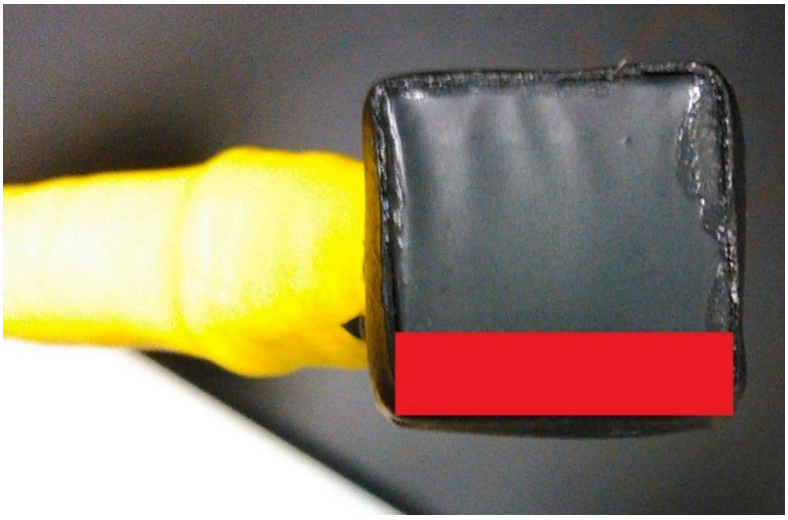

Figure 5-25 The inactive area of the camera at one end (at the third data point in Figure 5-24, equivalent to 5 mm).

Chapter 6 Development of GEM

As we briefly introduced in chapter 1 the current configuration of the GEM readout board is inappropriate for the high resolution needed for imaging. Here more details are discussed using the readout circuit shown in Figure 6-1.

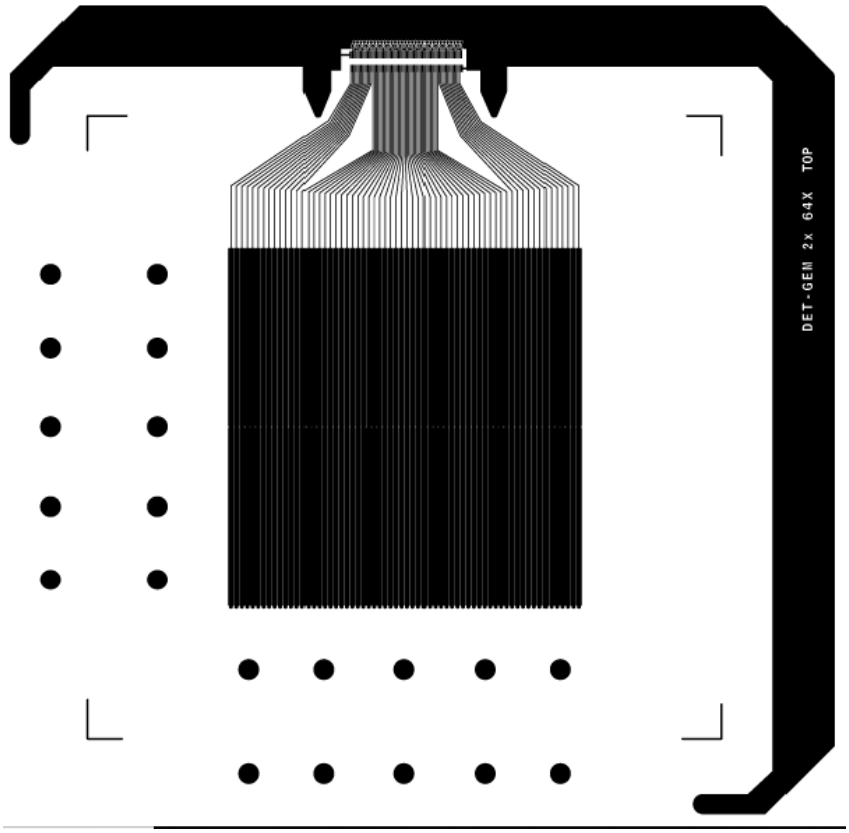

Figure 6-1 Current 3 layer GEM readout board

As we can see from Figure 6-1, there are 2 columns of 62 copper strips which would lead to a spatial resolution of ~1.6mm in the x direction, which is in line with the current beta camera we have tested. For the y direction, the resolution is on the scale of 5cm, too low to be used.

There are several ways to improve the resolution. Among them, the most obvious solution is to use the readout board with two layers of 128 strips. Each layer is tied to a specific

axis and the time delay between these interactions allows for the identification of the position of the interaction. A second redesign possibility is to have square detector elements placed in an array similar to the beta camera we have investigated. For higher resolutions we have to reduce the size of the detector elements, leading to a higher spatial density of pixels. If the current readout board is the only option, we can construct a translation or rotational scan base to covert the 1D data acquisition to 2D imaging. However, this remedy will suffer the long imaging time.

The next problem occurs from the triggering of the GEM to begin taking data. Currently we are using two photomultiplier tubes, PMT's, as a coincidence trigger with the GEM sandwiched between them on a delay to begin collecting data as shown in Figure 6-2. This puts a barrier between the GEM and the radiation source, meaning the emitted energies of the source need to be higher for the GEM to properly detect them. However, it is possible to augment the current voltage divider to allow for the GEM to self-trigger. This can be accomplished by adding a capacitor to the circuit after the last foil used effectively creating a low pass filter to pick-up on electrons that hit the copper on the top of the foil.

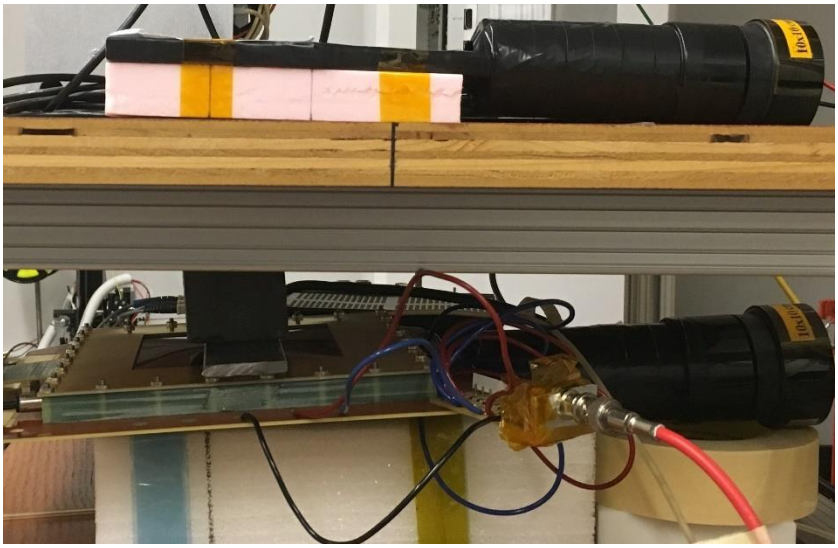

Figure 6-2 Basic trigger set-up of the GEM

The final problem comes from the readout code. An older variation of the AMORE code created by the RD51 collaboration is used currently, which can only run on a scientific Linux 5. It poses limitations on computation time and the use of the computer. In order to fix this problem, a new version of data acquisition code needs to be developed. The other possible solution is to use the newer versions of AMORE, however some of the functionality would have been lost, specifically the functions that could directly lead to imagining, such as event positions. Additional codding is needed.

Once these issues have been resolved then we can begin testing the medical imaging capabilities of the GEM's by repeating the experiments in the previous chapters before moving on to in vivo imaging.

Chapter 7 Future Work

While the results demonstrated in this work appear promising for future investigation, there are a few aspects of the camera which need to either be fixed or clarified. The first issue is the discrepancy between image collection times for varying source values, which created questions for both the uniformity test and the Field of View test. Additionally, a retest of the Field of View may be necessary to remove the discrepancy we noted in the results section.

For future experimentation on the beta camera we are looking into imaging of tumors in animals and comparing the required activity for the image and scaling up to human imaging. Additionally, we are planning on investigating possibly mounting the beta camera on a recently procured robotic arm and tying the image from it to an Ensenso 3-D camera in order to project the images collected from the beta camera into a structural 3-D image from the 3-D camera. Although some advance image processing and analysis is needed to incorporate two imaging modalities, this could greatly enhance the functional imaging rendered by the beta camera for a minimum invasive treatment of cancer.

Chapter 8 Conclusions

In this work we have provided a series of benchmark evaluations of a handheld beta probe for the surgical extraction of cancerous tumors and outlined the current state of development for GEM detectors for medical imaging. The results have shown a high degree of sensitivity across all pixels in the camera image. The 2-D image resolution is between 1 mm and 2 mm . However, we have also revealed an asymmetry between the spatial resolution in the horizontal vs. vertical directions through the use of the slanted-edge method for MTF calculation. Specifically, the spatial resolution in the horizontal direction seems to be ~20% lower than that in the vertical direction. Nevertheless the capabilities of the beta imager appear to be on par with similar devices in the field, therefor showing promise for radio-guided intervention.

For future experimentation on the beta camera we are looking into imaging of tumors in animals and comparing the required activity for the image and scaling up to human imaging. Additionally, we are planning on investigating possibly mounting the beta camera on a recently procured robotic arm and tying the image from it to an Ensenso 3-D camera in order to project the images collected from the beta camera into a structural 3-D image from the 3-D camera. Although some advance image processing and analysis is needed to incorporate two imaging modalities, this could greatly enhance the functional imaging rendered by the beta camera for a minimum invasive treatment and image-guided light-induced cancer therapy [17].

References

[1] T. Bates, “Benchmark Evaluation of a Hand-Held Beta Camera”

[2] IntraMedical Imaging LLC. “Beta Camera User Manual (Version 1.00)”

[3] L. Katz, “Range-Energy Relations for Electrons and the Determination of Beta-Ray End-Point Energies by Absorption”, Reviews of Modern Physics, January 1952

[4] F. Sauli “The gas electron multiplier (GEM): Operating principles and applications”, Nuclear Instruments and Methods in Physics Research, August 2015

[5] F. Sauli “Imaging with the gas electron multiplier” Nuclear Instruments and Methods in Physics Research A, 10 July, 2007

[6] A. Breskin, “The THGEM: A thick robust gaseous electron multiplier for radiation detectors” Nuclear Instruments and Methods in Physics Research A, 2 March, 2010

[7] K. Ljunggren, “Reduction of Noise in The Beta Camera for Low Activity Applications”, IEEE TRANSACTIONS ON NUCLEAR SCIENCE, August 1994

[8] E. Buhr, “Simple method for modulation transfer function determination of digital imaging detectors from edge images”, Proc. of SPIE Vol. 5030.

[9] M. O’Conner, “Quality Control of Scintillation Cameras (Planar and SPECT)”, AAPM

[10] Ammirati M, ‘Effect of the Extent of Surgical Resection on Survival and Quality of Life in Patients with Supratentorial Glioblastomas and Anaplastic Astrocytomas’.1987

[11] A. Terakawa, “A micro-pattern gaseous detector for beam monitoring in ion-therapy”, Nuclear Instruments and Methods in Physics Research B, 10, September 2015

[12] Masaoka K, ‘Modified slanted-edge method and multidirectional modulation transfer function estimation’ , 10, March 2014

[13] F. Liu, “A 64-pixel positron-sensitive surgical probe”, 2002 IEEE Nuclear Science Symposium Conference Record, 2002, pp. 1158-1162 vol.2.

[14] F. Liu et al., "Design and Performance of a Portable Positron-Sensitive Surgical Probe", IEEE MIC conference record, October 2000

[15] E. Hoffman, “Intraoperative probes and imaging probes”, Eur J Nucl Med (1999) 26:913–935

[16] Low-Beer B. Surface measurements of radioactive phosphorus in breast tumors as a possible diagnostic method. Science 1946; 104: 399.

[17] Jin et al., IEEE NSS MIC, 2013, 2014; Lai et al., QITJ, 2018

[18] Podgoršak E.B. (2009) Modes of Radioactive Decay. In: Radiation Physics for Medical Physicists. Biological and Medical Physics, Biomedical Engineering. Springer, Berlin, Heidelberg

[19] Jackson, “Electrodynamics”,2011

[20] SenseL, “An Introduction to the Silicon Photomultiplier”

Biographical Information

Thomas Bates received his bachelors degree in Physics from the University of Texas at Arlington in 2010, and was awarded his Masters in 2018 from the University of Texas at Arlington.

Since 2007 he has be involved in various research areas including Positron induced Auger Electron Spectroscopy (PAES) for surface characterization of topological insulators, as well as density functional theory approximations of the equilibrium magnetic configuration and volume of α-Plutonium. He has also been involved in solid rocket engine plume characterization at changing atmospheric pressure for thermal detection and imaging in the Fraunhofer region, and utility analysis of a potential future government projects at his job in the defense industry from 2010 to 2011. His current research in medical imaging devices will allow for advancement in the fields of tumor localization within the body for surgical extraction. For future interest he would like to pursue research in the field of quantum optics for brain mapping.